

SEISMOLOGY AND SPACE-BASED GEODESY

David M. Tralli

Earth and Space Sciences Division
Jet propulsion Laboratory, California Institute of Technology
4800 Oak Grove Drive, MS 183-501
Pasadena, CA 91109
Tel. (818) 354-1835
FAX (818) 393-5059

and

Fumiko Tajima

Institute for Geophysics
The University of Texas at Austin
8701 North Mopac Boulevard
Austin, TX 78759
Tel. (512) 471-6156
FAX (512) 471-8844

September 11, 1992

Accepted for publication in *Advances in Geophysics*

TABLE OF CONTENTS

1. Introduction	2
2. Seismological Measurements of Displacement	3
2.1 Characterization of Earthquake Source Parameters	3
2.2 Seismicity , Cumulative Moment Release, and Seismic Slip	6
3. Fault Models and Surface Deformation	7
3.1. Dislocation Theory	8
3.2. Uniform Halfspace Models	8
4. Spectrum of Crustal Strain Rates	10
4.1 Fault Friction Constitutive Relations	11
4.2 Preseismic Strain	12
4.3 Coseismic Strain	12
4.4 Post-Seismic Strain	13
4.5 Fault Creep	13
4.6 "Slow" and "Silent" Earthquakes	14
4.7 Rupture Nucleation Zone	14
5. Simultaneous Inversion of Seismic and Geodetic Data	15
5.1 Geodetic and Seismic Moments	15
6. Space-Based Geodetic Techniques	16
6.1 Very Long Baseline Interferometry (VLBI).....	18
6.2 Satellite Laser Ranging (SLR)	18
6.3 Global Positioning System (GPS).....	18
7. Geodetic Constraints on Large-Scale Seismological Problems	19
7.1 Regional Geodetic Baselines and Tectonic Plate Motion	19
7.2 Subduction Zones	20
7.3 Earth Orientation	20
7.4 Core-Mantle Coupling	20
7.5 Ionospheric Coupling of Seismic Sources	21
8. Continuously-Operating GPS Networks	21
8.1 Localized Strain Monitoring	22
8.2 Collocation with Seismographic Networks	24
9. Conclusions	25
References	26
Figure Captions	33

1. Introduction

The spatial and temporal distributions of strain accumulation and release involved in various tectonic and earthquake processes can be inferred from high-precision geodetic measurements of the corresponding **crustal** deformation at the Earth's surface. Space-based geodetic measurements which include the use of earth-orbiting satellites provide a significant contribution to understanding dynamic processes. This is due not only to the data quality but also to the **wealth** of information provided by the nature of such measurements and the error sensitivity to modeling **global geophysical** parameters. Unlike traditional ground-based geodetic techniques, such as **trilateration**, triangulation, and leveling, space-based geodesy yields simultaneous three-dimensional absolute positioning in an earth-centered reference frame. Space-based geodetic measurements can be of high spatial and temporal resolution, and also can ensure long-term temporal stability over **local** to regional and global distances.

The observable signals in space-based geodesy are emitted from **extragalactic** radio sources, as in very long baseline **interferometry (VLBI)**, from earth-orbiting satellites of the Global Positioning System (GPS), or are ground-based signals reflected from specialized earth-orbiting satellites and from **retroreflectors** emplaced on the moon, as in satellite laser ranging (SLR) and lunar **laser** ranging (LLR), respectively. A distinctive advantage of space-based geodesy over ground-based measurement techniques is that the receiver stations need not be mutually visible, greatly enhancing the capability of understanding deformation processes over greater distances. Strain rates are determined from changes in the relative positioning estimates of geodetic baselines connecting pairs of ground-based receivers within a network of established sites. These sites are occupied periodically, or continuously in **local** deformation monitoring applications and in permanent regional or global networks. Three-component strain and tilt estimates in principle can be integrated in a self-consistent manner over a broad range of **length** scales, **locally** from seismic source dimensions to globally for **tectonic** plate interaction studies.

The acquisition of geodetic data on regional and global scales allows direct estimation of tectonic **plate** motions, which presumably are constant over the time span of geodetic **measurement** programs. In conjunction with geologically and **geophysically** determined slip rates, if available, slip rate and azimuth estimates obtained from the inversion of geodetic data can be compared with values estimated from **cumulative** seismic moment release to assess the proportion of seismic to tectonic slip. Such a comparison gives insight into the dynamics of tectonic and seismic processes and their interrelationship for accommodating the accumulation of strain. Larger-scale measurements have yielded plate motion estimates that are consistent with those obtained from **paleomagnetic** data [DeMets *et al.*, 1990] in some regions. Smaller-scale measurements are evolving rapidly from dealing primarily with the empirical assessment of measurement precision and long-term stability (accuracy), particularly for comparison with well-established geophysical measurement techniques, to yielding scientifically viable results [e.g. Larsen *et al.*, 1992; Shimada and Bock, 1992; Genrich and Bock, 1992].

In this paper, we explore the potential of space-based geodetic measurements of crustal, or more **generally lithospheric**, deformation in the context of seismology. Geodetic measurements made at various phases of the earthquake cycle for a given fault, if incorporated with earthquake source characterization analyses, geometrical **fault** models, and mechanical models of fault zone behavior, may lead to improved **parameterization** of strain accumulation, release, and relaxation in the earthquake source region. The driving forces in these models are constrained by regional plate motion estimates. High-precision space-based geodetic measurements are an exciting complement to local and broad band regional seismology. Mechanical conditions of plate boundary deformation can be modeled comprehensively only by integrating local and regional **measurements**. Since deformation measurements on complementary length scales and with overlapping response are required in order to develop consistent dynamic and kinematic models of crustal and lithospheric deformation.

Our intent is to review the **achievements** of seismological source theory and data analyses, mechanical modeling of fault zone behavior, and advances in **space-based** geodesy, and to focus on what we feel are realizable contributions of space-based geodetic **measurements** specifically to the field of seismology. We summarize the fundamental relationships between the **crustal** deformation associated with an earthquake and the geodetically observable data. Throughout this paper, we stress the response and spatial and temporal resolution of the geodetic data required to understand deformation at various phases of the earthquake cycle. In addition, we discuss the use of VLBI, SLR, and GPS **measurements** for studying global geodynamic properties that can be investigated to some extent with seismic data. Finally, we evaluate the potential **con-**

tributions of continuously operating strain monitoring networks and globally distributed geodetic observatories to existing worldwide modern digital seismographic networks, in view of mutually addressable problems in seismology, geophysics, and tectonics.

2. Seismological Measurements of Displacement

The accumulation of tectonic stress leads to earthquakes whose occurrence, in turn, results in the accommodation and release of such tectonic stress. The accumulation and release of tectonic stress can be investigated in relation to an earthquake cycle defined by **preseismic**, **coseismic**, post seismic, and inter seismic phases. During each of these phases the **crustal** deformation exhibits a characteristic behavior [Thatcher, 1975]. However, neither the spatial extent of strain release near the source and at the surface nor the time frame of corresponding deformation signatures is fully understood [e.g. *Mavko*, 1981]. Geodetic measurements spanning the earthquake process with high spatial and temporal resolution and long-term stability may contribute to studies of **crustal** deformation, allowing the consistent integration of strain measurements from time scales of a few minutes before rupture to several years before and after significant earthquakes, and over distances comparable to seismic source dimensions and entire plate boundary deformation zones. Figure 1 illustrates length scales and time spans **pertinent** to major earthquakes ($M > 6$) and space-based geodetic measurements, including the dimensions and time spans associated with pre seismic and **post** seismic deformation, which are yet ambiguous.

Ground motions resulting from an earthquake are recorded by seismographic instruments on the Earth's surface, yielding seismograms, or waveform records, spanning a broad temporal spectrum from below 1 s for body waves to over 300s for surface waves. Free oscillation data for large earthquakes also may be obtained from the very-long-period instruments. The various seismic waveform data are analyzed in order to characterize the earthquake source process as a series of displacements on a given number of fault surfaces. **Seismicity** is increasingly time-variant over shorter observation spans and leads to **crustal deformation** with comparably varying temporal signatures manifesting the accumulation and relaxation of strain. The surface deformation caused by an earthquake source rupture at depth can be observed geodetically as instantaneous static displacements in the near-field, **More subtle** surface deformation, associated with pre seismic strain accumulation and premonitory displacements, and post seismic viscoelastic relaxation, also may be observed geodetically in the vicinity of the earthquake epicenter provided that such measurements are of sufficient resolution and that signals themselves exist.

2.1 Characterization of Earthquake Source Parameters

In this section, we review briefly and from a practical viewpoint the representation formulas of displacements caused by an earthquake, as derived by *Haskell* [1964, 1969]. We explain how these representations are used to model recorded body waveforms or to estimate source characteristics using an inversion method. Static (**geodetic**) and kinematic (seismic) data of comparable frequency response can be inverted simultaneously in order to determine earthquake source model parameters. The contributions of surface geodetic data primarily take the form of constraints on the lower frequency source spectra, thereby allowing the integration of **local** and regional surface deformation measurements, and yielding better determination of deep fault slip, differentiation of aseismic creep, and continuous imaging of the processes leading to and following ruptures. **Surface** geodetic data thus may help evaluate various realistic fault models and constitutive relations developed from laboratory measurements of rock samples.

2.1.1 Earthquake Source Modeling

Displacements observable at the Earth's free surface can be computed by numerical integration of the Green's function which describes the displacements, caused by a finite earthquake source, over space and time for a given medium. The Green's function depends on the source and observation (**receiver**) coordinates and time, and satisfies **boundary** conditions on the fault surface, A , which are specified by the particular problem (see Fig. 2a for the source and observation geometry). The **elastodynamic representation** theorem in the form given by *de Hoop* [1958] provides the mathematical basis for such a calculation,

$$u_i(x_1, x_2, x_3, t) = \iiint_V G_{ij} f_j dV + \iint_A c_{jk, pq} G_{ij} [\partial u_p / \partial \xi_q] n_k dA + (\partial / \partial x_q) \iint_A C_{jk, pq} G_{ip} [u_j] n_k dA \quad (2.1)$$

where x_1, x_2, x_3 are the Cartesian coordinates of the point at which the displacement component u_i is to be evaluated, ξ_1, ξ_2, ξ_3 are the Cartesian coordinates of the point of integration in V and on A , and f_j is a body force per unit volume, and

$$c_{jk, pq} = \rho (\alpha^2 - 2\beta^2) \delta_{jk} \delta_{pq} + \rho \beta^2 (\delta_{jp} \delta_{kq} + \delta_{kp} \delta_{jq})$$

where ρ is density, α and β are the compressional and shear wave velocities, respectively, and δ_{mn} is the Kronecker delta (see *Haskel [1964]* for further parameter descriptions). G_{ij} transforms a given function $\phi(\xi_1, \xi_2, \xi_3, t)$, which describes the rupture propagation, into

$$G_{ij}[\phi(\xi, t)] = (4\pi\rho)^{-1} \{ (3\gamma_i \gamma_j - \delta_{ij}) r^{-3} \int_{r/\alpha}^{r/\beta} \phi(\xi, t - t') t' dt + \gamma_i \gamma_j (\alpha^2 r)^{-1} \phi(\xi, t - r/\alpha) - (\gamma_i \gamma_j - \delta_{ij}) (\beta^2 r)^{-1} \phi(\xi, t - r/\beta) \} \quad (2.2)$$

where r is the distance from (ξ_1, ξ_2, ξ_3) to (x_1, x_2, x_3) , and

$$\gamma_i = (x_i - \xi_i)/r$$

A form of this theorem appropriate for the representation of a faulting source in an infinite homogeneous medium is given by *Haskel [1964]* as follows:

$$4\pi \dot{u}_i(x, t) = 2(\beta/\alpha)^2 \iint_{A^+} (\alpha r)^{-1} \gamma_i \gamma_1 \gamma_3 \ddot{D}(\xi, t - r/\alpha) dA + \iint_{A^+} (\beta r)^{-1} \{ -2\gamma_i \gamma_1 \gamma_3 + \gamma_3 \delta_{i1} + \gamma_1 \delta_{i3} \} \ddot{D}(\xi, t - r/\beta) dA \quad (2.3)$$

where $D = u^+ - u^-$ is the relative displacement on the A^+ surface with respect to the A^- surface. Furthermore, *Haskel [1969]* computes displacement, particle velocity, and acceleration waveforms in the near-field of a propagating fault by numerical integration of the Green's function integrals for an infinite medium.

Waveform data from an earthquake source usually are more complex than predicted from a simple fault model. Many seismologists have developed methods to model a complex earthquake source using body waveforms. Given the limited extent of this paper on this topic, we refer to the iterative inversion method which has been developed systematically by *Kikuchi and Kanamori [1982; 1986; and 1991]* to model a source rupture process with a series of point sources. Using this method, the far-field body waveform is modeled with a superposition of waveforms from the various point sources. From Eq. (2.3), the far-field body waveform due to a shear dislocation source is described in a simple form by

$$U_c(x, t) = \frac{Rc\mu}{4\pi\rho c^3 r_0} \iint_A \vec{D}(\xi, t - r/c) dA \quad (2.4)$$

where ξ is a variable point on A , r is the average of the distance r to the rupture front, $D(\xi, t)$ is the relative slip velocity, R_c is the radiation pattern, ρ is density, μ is rigidity, and c is the body wave velocity [*Kikuchi and Kanamori, 1982*]. Assuming that the travel time r/c can be approximated by its average value, r_0/c , the body waveform is given by,

$$U_c(x, t) = \frac{Rc\mu}{4\pi\rho c^3 r_0} S(t - r_0/c) \quad (2.5)$$

where the $S(t)$ is the far-field source time function defined by

$$S(t) = \mu \iint_A \dot{\vec{D}}(\vec{\xi}, t) dA. \quad (2.6)$$

If the rupture propagation is characterized by abrupt changes in the fault area expansion rate, then the source time function $S(t)$ is given by a superposition of ramp functions,

$$S(t) = \sum m_i s(t - \tau_i) \quad (2.7)$$

where $m_i = \Delta A_i$, ΔA_i is the increment of the fault area expansion rate at time τ_i , and

$$s(t) = \begin{cases} 0 & t < 0 \\ t/\tau & 0 \leq t \leq \tau \\ 1 & t > \tau \end{cases}$$

In the inversion, subevents ordered by magnitude are determined in a least-squares sense, and thus an earthquake source rupture is described as a series of **subevents** which are distributed on a single fault or faults (see Fig. 2b). We should note that in the early version of this method [Kikuchi and Kanamori, 1982; 1986] the fault mechanism of each point source, or subevent, was fixed during the inversion and only the spatial distribution and onset times of point sources on the given fault surface(s), as well as the point source magnitudes, were determined to account for the source complexity. In the recently improved version of this method [Kikuchi and Kanamori, 1991], the constraint of a single or multiple fixed fault mechanism can be relaxed and the moment tensor of each subevent can be determined from the inversion. With more variable parameters, the inversion may become more unstable and require certain constraints in order to obtain reliable resolution.

Recently, some studies have attempted to use strong motion waveform data and geodetic data simultaneously in an inversion [e.g. Yoshida and Koketsu, 1990]. While typical geodetic data do not provide temporal information for characterization of the rupture process (although the potential for such exists, as we shall discuss in Section 8), these data are adequate for constraining the fault slip distribution in the low frequency range. The actual source rupture process is complicated by heterogeneous mechanical properties and possible nonlinear strains [e.g. Vasco et al., 1988]. For example, a continuous increase of rigidity with depth increases the shear strain near the fault surface, as was pointed out by Mahrer and Nur [1979].

2.1.2 Moment Release

The amount of coseismic strain release, corresponding in large part to the strain accumulated during an inter seismic period, can be estimated using the relations between displacements (D), seismic moments (M_0), and strain energy (E) [see Kanamori and Anderson, 1975]. The change in strain energy (ΔE) due to a change in the static stress field ($\Delta \sigma$) from σ_0 to σ_1 is given by

$$\Delta E = A \cdot \bar{D} \cdot \bar{\sigma} \quad (2.8)$$

where \bar{D} is the average fault offset, or relative displacement, and $\bar{\sigma}$ is the mean stress drop. Since the total seismic moment is the fault surface integral (or summation for a discretized fault model) of the product of the relative displacement and rigidity, the strain energy is linearly proportional to the seismic moment. The average fault displacement also is proportional to the coseismic stress drop (see the summary for different fault types by Kanamori and Anderson [1975]; e.g., for circular faults [Eshelby, 1957; Keilis Borok, 1959], for shallow infinite strike slip faults [Knopoff, 1958], and for shallow infinite dip slip faults [Starr, 1928; Aki, 1966]). Linearity ensures that the rate of coseismic strain energy change is related to the fault slip rate.

A spatially and temporally averaged fault traction therefore maybe defined, and the strain energy release rate may be estimated from the fault displacement or tectonic plate motion rate. Relevant surface strain rate data for the fault then can be integrated to estimate the time required to recover coseismic strain

during the inter seismic period. This corresponds to the “time-predictable” model of earthquake recurrence, which is based on **coseismic** strain drops and average strain accumulation rates [Shimazaki and Nakata, 1980; Sykes and Quittmeyer, 1981]. When baselines for geodetic measurements are established adequately in relation to an earthquake **fault**, the displacement rates of the two baseline endpoints can be used to derive strain rates. Thus, geodetic displacements and strain rates similarly are linear functions of fault slip rate. Segall and Harris [1987] apply this approach to **trilateration** data at Parkfield, California.

2.2. Seismicity, Cumulative Moment Release, and Slip Estimates

The seismic moment released during an earthquake is the predominant portion of the strain energy accumulated since the previous earthquake in the source region. The seismic slip rate can be estimated from the total released moment. However, the slip adjustments may be **aseismic**, in which case the ratio of seismic to tectonic slip would be too small. Regional geodetic measurements help quantify the complementary nature between seismic and **aseismic** slip. The availability of both seismic and geodetic measurements provides insight into the mechanical conditions of plate boundary deformation, and the distribution of relative displacements and strain. Unlike traditional geodetic measurements, space-based measurements allow the estimation of slip rates on baselines which may span the entire width of a plate boundary deformation zone, and in principle, in a self-consistent manner for comparison with localized deformation if the geodetic network is designed with a range of appropriate baseline lengths. However, in practice this path integration of strain is difficult to achieve because vertical geodetic resolution is worse than horizontal and relative position errors increase with baseline length.

2.2.1 Estimation of Seismic Slip

Seismic slip rates are estimated from the accumulated seismic moment release assuming typical fault parameters for events in the area of interest. Generally, the seismic slip of an active fault region is estimated according to the formula given by Brune [1968]. The average slip over a fault surface ($\langle u \rangle$) is expressed as

$$\langle u \rangle = M_0 / (\mu A) \quad (2.9)$$

where M_0 is the seismic moment, μ is the rigidity, and A is the area of the slip. If we let the average slip extend over the entire fault area (A_0), then

$$\langle u \rangle = \frac{A}{A_0} \langle u \rangle = \frac{A}{A_0} \frac{M_0}{\mu A} = \frac{M_0}{\mu A_0} \quad (2.10)$$

and the total slip (U) is obtained as

$$U = \sum \langle u \rangle = 1/(\mu A_0) \sum M_0. \quad (2.11)$$

The depth extent of a fault generally may be somewhat ambiguous, determined in gross by the average **crustal** thickness or earthquake sequence source depths.

2.2.2 Seismicity and Cumulative Moment Release

Variations in spatial and temporal **seismicity** patterns have been studied by many authors. Tajima and Tralli [1991], for example, used the simple relations outlined above to consider the correspondence between space-based geodetic measurements of Pacific-North American relative plate motion in the Gulf of California and seismic slip estimates from centroid moment tensor solutions, and to ascertain whether variations in geodetically estimated tectonic slip rates may be attributable to the pattern of seismicity in the region. Tajima and Tralli [1991] found that the seismic to tectonic slip ratio in the gulf is between approximately 17 and 30?40 but appears to increase slightly from south to north, progressing in the transition from oceanic to continental transform system along the plate boundary. If **seismicity** reflects the accommodation of plate motion, then geodetic measurements of relative motion across different sections of a tectonic plate

boundary similarly may be expected to vary about an average angular velocity (for a given pole of rotation) due to local boundary zone complexities.

In order to ensure that geodetic and seismic measurements lead to a well-constrained and consistent model of tectonic plate interaction, the effects of **plate** boundary zone complexities and non-rigid plate behavior must be identified. Space-based regional measurements are invaluable in this regard. Geodetic measurements of relative plate motion can be disturbed by short-term **effects** associated with episodic **seismicity**. To assess such effects, *Tajima and Tralli* [1991] used a simple dislocation model (Section 3.1) to estimate the surface displacements due to typical **large** transform events in the gulf (see Figs. 7 and 8). In the advent of increasing precision in regional measurements, their results show the importance of considering whether major earthquakes with significant seismic slip can affect geodetic estimates of relative plate motion, or conversely, whether geodetic errors are sufficiently low to resolve episodic slip in long-term measurement programs. We shall return to these issues later.

3. Fault Models and Surface Deformation

In the previous section, the relationship between surface deformation and seismic source characteristics was summarized using representation formulas. Differences between seismic slip estimates and geodetic estimates of tectonic slip also were discussed. We noted that geodetic baselines spanning a plate boundary must be insensitive to boundary effects associated with local **seismicity** in order to obtain an unperturbed estimate of the overall relative plate motion. However, if the interest lies in studying the mechanical behavior of the plate boundary, which is manifested as a system of faults for example, shorter baselines must be measured with the intent of resolving the near-field deformation. This transition in characteristic length scale, from source dimensions out to a **few** fault widths, will be used now to discuss surface deformation modeling associated with seismic slip.

Repeated slip dislocations, or fault displacements, lead to the accumulation of surface deformation, and hence to the evolution of **geomorphologic** features [e.g. *King et al.*, 1988]. This follows from Eq. (2.1 1) upon superimposing the slip associated with a series of events on the same **fault** plane. The rates of these **deformational** processes can be estimated geodetically. The stress relaxation time, determined by the viscosity of the medium, and the wavelength of the deformation both must be long enough so that the surface deformation associated with fault rupture is not absorbed rapidly by an elastic-ductile lithosphere [*King et al.*, 1988]. The accumulated deformation may be observed during long-term geodetic programs that ensure measurement stability over local to regional distances. The onset of rupture and the earthquake source properties are **determined with** seismic data, although the latter may be constrained with geodetic **measurements**, as we shall discuss in Section 5.

The ability to resolve the subtle spatial and temporal behavior of viscoelastic deformation is limited by the **level** of precision attainable with geodetic measurements at the surface. Admittedly, much of the focus of space-based epoch (periodic) geodetic **measurements** and continuous monitoring networks to date has concentrated on the determination of far-field displacements associated with rigid plate motions corresponding to linear or uniform slip rates. To be fair, in large part this has been the result of a desire to compare and develop global plate motion models and a need to **verify** the various geodetic systems, and (albeit decreasingly) of economic limitations imposed by the unavailability and cost of receivers for dense networks, and (decreasingly) the technological limitations imposed by error sources that are not characterized fully. These factors compromise the applications and potential resolution of the measurements over shorter distances where more complex deformation perhaps could be imaged. However, geodetic measurements at a local scale have increased [e.g. *Shimada and Bock*, 1992; *Genrich and Bock*, 1992].

Although simple fault models often predict quite adequately the deformations geodetically observed at the surface, our intent here is to provide a simple framework that **allows** the **reader** to realize the potential of high-resolution space-based geodesy for constraining realistic models of deformation, particularly in conjunction with broad band seismological **measurements** and other high-resolution strain measurement techniques. We emphasize that the various measurement types are complementary and of overlapping long-period deformation response. Advances in understanding seismic and tectonic processes can be gained through modeling the various measurements simultaneously to yield a broad, integrated, and consistent characterization of the spatial and temporal properties of the deforming medium and the causative sources.

3.1 Dislocation Theory

Simple fault models can be used to calculate three-dimensional surface displacements given a slip dislocation at depth. In this section we review expressions of surface slip as a function of distance from the fault, assuming simple strike-slip geometry. Elastic and viscoelastic models are discussed in the context of inverting geodetic data of high temporal resolution, eliminating the potential aliasing of shorter-period deformation signals [e.g. *Tralli, 1991*] and allowing the imaging of post seismic relaxation phenomena.

A shallow, strike-slip, vertical fault may be modeled mathematically by a simple screw dislocation which yields a corresponding static displacement. Consider a circular source of radius $r = (x^2 + y^2)^{1/2}$ centered on the dislocation axis (z) at a depth $y = D$ below the free surface of an infinite medium (**Fig. 3**), where the (x,y) plane is perpendicular to the fault (Burgers vector is on the fault plane at depth D in the z direction). The shear strain (ϵ_{yz}) on a fault-parallel plane ($x = \text{constant}$) is the resolved component of the uniform shear strain about the circle and is equal to $S/2\pi r \cdot (y/r)$, where S is the displacement on the fault surface. The surface shear strain across any plane parallel to the fault can be integrated to give the fault-parallel displacements (u) of surface points

$$u(x, D) = \int_{-\infty}^x \epsilon_{xy} dx = \frac{S}{2} \left(1 - \frac{2}{\pi} \tan^{-1} \frac{x}{D} \right) \quad (3.1)$$

(see *Stacey* [1977] for further discussion). This is the familiar inverse tangent relationship which yields the surface deformation as a function of dislocation depth (D) and perpendicular distance (x) from the fault, and which can be observed geodetically [*Savage and Burford, 1973*]. A greater depth of faulting results in a greater perpendicular distance from the fault at which the surface deformation can be observed readily. For example, assume that D is 10 km and that the geodetic resolution is 1 part in 10^7 over a 100 km baseline centered perpendicularly across a fault. A static surface slip of about 5 cm on the fault can be resolved, yielding displacements of 5 mm in opposite directions at each baseline endpoint (the relative baseline displacement is thus 1 cm); if D is 15 km, about 5 cm of slip at the fault surface can be resolved. The shear strain rate for a dipping fault is obtained by replacing x with $x - D \cot \delta$ in the expression for fault-parallel shear strain, where δ is the fault dip [*Savage, 1983a*], and the corresponding fault-parallel slip then follows from the integral in equation (3.1).

3.2 Uniform Halfspace Models

A simple two-dimensional fault model typically is represented as a slip plane in a uniform halfspace or in a layer over a uniform halfspace (**Fig. 4**). In either case, the stress that drives the motion on the fault is associated with the far-field plate motion. If the fault is specified as a slip plane in an elastic layer (lithosphere) over a viscoelastic halfspace (asthenosphere), the stress diffusion between lithosphere and asthenosphere [*Elsasser, 1969*] determines the distribution of fault displacements, the fault being locked during stress accumulation while the system is driven by the tectonic plate motion [*Turcotte and Spence, 1974*]. The distance over which stress will diffuse in time t is given approximately by

$$(\mu h_a H / \eta)^{1/2} \quad (3.2)$$

where μ is rigidity, H is the lithospheric thickness, and h_a and η are the asthenosphere thickness and viscosity, respectively [*Bott and Dean, 1973*]. Typical parameter values yield diffusion distances of a few hundred kilometers. *Rydelek and Sacks* [1989] show that fault slip and viscosity can be determined from geodetic data collected several years after an earthquake, given dispersive stress propagation with velocities ranging from 1 to 10 km/yr.

Dislocation models in an elastic layer over a viscoelastic halfspace predict that strain accumulation and release occur over dimensions much greater than those predicted by halfspace models due to the long-term viscoelastic propagation of stored strain energy [*Cohen, 1982; Ward, 1985*]. Furthermore, numerical modeling of two-dimensional strike-slip faults suggests that high asthenosphere viscosity results in constant inter seismic strain accumulation, wherein lower viscosity results in decreasing strain accumulation [*Turcotte et al., 1979*]. Therefore, we see that high-resolution surface deformation measurements can be

used to infer fault rheology, much in the same way that **well-determined** vertical deformation measurements may be used to test **asthenosphere** relaxation models and post-glacial rebound, where the **flexural** rigidity of the crust can be described by an effective elastic thickness. The advantage of space-based geodetic **measurements** for addressing these types of problems lies in regional spatial coverage and long-term measurement stability in an absolute global **reference** frame.

3.2.1 Equivalent Elastic *Halfspace*

Savage [1990] suggests that an appropriate lithosphere-asthenosphere model for a slip dislocation may be constructed from the parameter values for an equivalent slip dislocation in an elastic **halfspace** obtained from the inversion of geodetic data. In the depth range between 0 and H , where H is the thickness of the elastic layer over a **viscoelastic halfspace** (e.g. Fig. 4), the equivalent elastic **halfspace** model yields a coseismic slip of VT with no slip in the inter seismic interval, thus prescribing an earthquake cycle. V is the uniform slip rate given by the secular relative plate motion occurring on the fault below a depth H , above which the fault is locked, and T is the time interval between earthquakes. The velocity field on the free surface is given by differentiating Eq. (3.1). At distances greater than $10H$ from the **fault**, the slip velocity is $(\delta S/\delta t)/2$. In depth intervals **below** H , the slip rates in the equivalent **halfspace** model are given by

$$F_n(t) \exp(-\mu t/2\eta) \quad (3.3)$$

for $(2n-1)H < y < (2n+1)H$, where μ is the rigidity or shear modulus, η is the Maxwell viscosity in the **asthenosphere** model, and t is the time since the last earthquake. The coefficients $F_n(t)$ are $(n-1)$ degree polynomials that depend on the ratio of time (t) to relaxation time $(2\eta/\mu)$, on t/T , and on V (which is the average slip rate in each depth interval) [see *Savage*, 1990]. Although surface slip rate data could be inverted to obtain the slip distribution at depth, the high correlation between the depth intervals and the decreasing resolution with depth in practice imply that an inversion actually may involve intervals of increasing thickness above an infinite **halfspace** [*Savage*, 1990].

3.2.2 Viscoelastic Deformation

Viscoelastic models indicate subtle differences in the spatial distribution of deformation compared to purely elastic models. The time scale of seismic wave propagation indicates that seismic data respond to the elastic properties of the medium, while longer-term geodetic displacement **measurements** may be able to observe **viscoelastic** relaxation if a minimum geodetic resolution of 1 part in 10^8 of baseline length is achieved. *Savage and Presto* [1978] construct a simple two-dimensional model of the earthquake cycle from the *Nur and Mavko* [1974] solution for a screw dislocation in an elastic plate (lithosphere) overlying a **viscoelastic halfspace** (asthenosphere) and draw three conclusions: (1) surface deformation due to **asthenospheric viscoelastic** relaxation cannot be distinguished easily from the effects of accelerated slip on a vertical fault in an elastic **halfspace**; (2) the effect of **asthenospheric** relaxation is important only if the depth of the seismogenic zone is comparable to the lithospheric thickness; and (3) the effect of lithospheric and **asthenospheric** coupling is to decrease the time span of postseismic deformation and to concentrate the region of significant strain change closer to the **fault** than in a purely elastic **halfspace**.

In this section, we consider some of the effects of **viscoelastic** deformation on high-resolution geodetic **baseline** measurements. We use the expressions given by *Rosenman and Singh* [1973] and *Singh and Rosenman* [1974] for obtaining quasi-static surface displacements, strains, and tilts from the simple case of a slip dislocation in a Voigt or Maxwell **viscoelastic halfspace**, as derived from the elastic solutions of *Chinnery* (1961) using the correspondence principle of linear viscoelasticity. The temporal dependence of **viscoelastic** deformation arises from the dilatational and shear relaxation functions which are integrated in the stress-strain relations [see *Turcotte et al.*, 1979], and are observed through the ratio of observation time (t) to relaxation time as in Eq. (3.3). Therefore, it is only over time scales of the order of the Maxwell relaxation time that **viscoelastic** behavior can be observed (for a Voigt model, the observation time must be considerably smaller than the relaxation time). Specifically, in the Maxwell model for example, the duration of geodetic measurement programs must be comparable to or less than the relaxation times in order to differentiate between elastic and Maxwell **viscoelastic halfspace** models. The equations **reduce** to the **corre-**

spending elastic case, namely the coseismic displacement, in the limit of t/τ approaching zero in a Maxwell viscoelastic halfspace or approaching infinity in a Voigt viscoelastic halfspace.

The simple fault model geometry is shown in Fig. 5. Only the amount of instantaneous slip and the length (L) and depth extent (h and H) of the rectangular fault plane need to be specified *a priori*. Surface displacements are linearly proportional to the amount of fault slip, as was shown in Section 2. The amount of estimated slip could be larger for a smaller fault dimension, and still yield an equivalent seismic moment (Section 2.2.1). The relaxation time of a Maxwell viscoelastic halfspace is $2\eta/\mu$, where η is the Newtonian viscosity and μ is the rigid body shear modulus [Savage and Prescott, 1978; Turcotte and Schubert, 1982, p. 337]. Estimates of asthenospheric viscosity for a tectonically active (continental) region, inferred from postseismic relaxation, are about 5×10^{19} Poise [Nur and Mavko, 1974]. Li and Rice [1987] examined geodetic strain data on the San Andreas fault and obtained values of 2×10^{19} to 1×10^{20} Poise for various depths of an elastic layer (lithosphere) over a viscoelastic halfspace (asthenosphere), assuming a lithospheric thickness of about 20 to 30 km. The corresponding relaxation times are 10 to 16 yr.

Some key aspects of viscoelastic deformation can be addressed with high-resolution space-based geodetic measurements. For example, the strain pattern due to a strike-slip dislocation changes according to the relaxation time of the medium, as shown in Fig. 6, and such changes are manifested within epicentral distances of about two fault lengths; the various models converge in the far-field. Furthermore, differences between elastic and viscoelastic halfspaces not only affect the magnitude of the surface deformation but also may introduce new nodal lines separating deformation of opposite sign [e.g., Singh and Rosenman, 1974], thus possibly changing the sign of the deformation measured between geodetic sites. Understanding the effect of viscoelastic deformation is important for the inversion and interpretation of geodetic measurements to constrain rheologic properties, although this is an inherently non-unique process. Figure 8 is based on an analysis by Tajima and Tralli [1991] which compares the surface displacements predicted by an elastic and Maxwell viscoelastic halfspace model for transform events in the southern Gulf of California (Fig. 7) with GPS geodetic resolution along a 450 km baseline (see figure captions). The results of their numerical calculations suggest that if a large transform event with a seismic moment of about 1.5×10^{26} dyne-cm were to occur within 100 to 200 km of a gulf-crossing baseline, the relative distance measurements could be affected by up to 15 mm. In addition, although the relative displacements shown in Fig. 8 are resolvable marginally only for event I, the effect of viscoelastic deformation is quite small (at the few millimeter level) and cannot be detected over long baselines which yield a zero net relative change.

Viscoelastic effects are manifested predominantly in the near-field, with some diffusion into the far-field. High spatial geodetic resolution of at least a few millimeters plus 1 part in 10^8 of baseline length thus is required, in addition to temporal measurement stability, to model non-rigid effects of plate boundary deformation and to differentiate between time-dependent models. This reiterates the interest in space-based geodetic measurements for estimating gross plate motions simultaneously with seismic measurements of local slip fluctuations, and for consistently integrating near-field and far-field strains in order to understand plate boundary mechanics.

4. Spectrum of Crustal Strain Rates

Strain rates associated with tectonic motion are of the order of 10^{-7} to 10^{-8} & yr^{-1} [Savage, 1983a]. At distances within a fault length, the strains are 10^{-6} E, within a factor of 100 of the maximum strains expected along the rupture surface ($\Delta\epsilon = \Delta\sigma/2\mu$, where $\Delta\sigma$ is the nominal stress drop, and μ is the shear modulus) [Wyatt, 1988]. Understanding this broad range of crustal deformation requires measurements with high spatial and temporal resolution, which we shall quantify in this section. Regional tectonic strain rates can be observed with periodic geodetic measurements. Thatcher [1975] suggests that strain accumulation prior to the April 18, 1906, San Francisco earthquake occurred over a period of about 50 yr, and aseismic strain release over a period of about 30 yr after the earthquake. However, problems in fault zone behavior, such as the depth extent of creep, its relationship to rupture, and the distribution of fault slip (during the entire seismic process) suggest that continuous surface deformation monitoring is desirable given the short periods which may characterize possible strain signals and the need to avoid aliasing precursory deformation signatures [Tralli, 1991], as for example in earthquake and volcanic eruption prediction programs.

We discuss the various strain rates associated with regional tectonic deformation, represented largely by the intersismic period of the earthquake cycle, and the strain rates associated with preseismic, coseismic,

and postseismic deformation. These latter phases of the earthquake cycle, which are related more directly to the acceleration and release of strain energy during rupture, have implications for short- and intermediate-term earthquake prediction programs. Nonetheless, interseismic strain accumulation must be understood in order to detect anomalous behavior in intermediate-term prediction. We show, through the results of published laboratory studies of rock behavior and the corresponding development of constitutive relations, that high-resolution space-based geodetic measurements may contribute significantly to the understanding of the earthquake rupture process, and to constraining dynamic and kinematic models of strain accumulation and release.

4.1 Fault Friction Constitutive Relations

The relationship between stress and strain is known as the constitutive relation, and is a function of the material properties of the medium. Constitutive relations are important for determining the amount of deformation expected from the application of a given stress field, and for the inversion of geodetic data related to fault slip. Increasingly, laboratory studies of rock samples have been improving our understanding of the frictional properties of fault surfaces and the corresponding temporal distribution of strain and slip at the point of rupture. If geodetic measurements of crustal deformation also are to contribute to studies of fault zone behavior, then their resolution must be such that constraints may be placed on realistic fault models rather than on simple uniform halfspace models. Fitting local geodetic measurements to simple deformation models is useful for testing the consistency of the measurements themselves and for isolating the gross deformation features associated with rupture. However, such measurements are of little interest to the seismological and geophysical communities if their spatial and temporal resolutions are inadequate for providing further constraints on realistic parameter inversions. In this regard, knowing which seismological problems involve greater uncertainties (e.g. fault zone behavior) steers the development and application of geodetic techniques in a manner which helps constrain the solutions to these problems. In the following sections we focus on deformation behavior close to the fault in the context of preseismic, coseismic, and postseismic strain changes, and discuss how high-resolution space-based geodetic measurements may enhance the imaging of surface deformation for inferring earthquake source parameters.

The constitutive behavior of faults can be described by the response to a step increase in sliding velocity, whereby the initial effect is an increase in frictional resistance followed by an exponential decay of frictional resistance over a characteristic length of slip displacement that scales with surface roughness or asperity. If the decay is greater than the initial frictional resistance increase, the material is weakened ("velocity weakening"), and if the decay is less the behavior is termed "velocity strengthening" [Tullis, 1988]. Creeping (stable) and locked (unstable) segments of faults may be described by materials that strengthen or weaken, respectively, in response to stress loading.

"Stick-slip" instability depends on whether frictional resistance decreases more rapidly than the driving force. The ratio of the coefficient of static friction, μ_s , to that of stick-slip or kinematic friction, μ_k , may be expressed as

$$\frac{\mu_s}{\mu_k} = \frac{Q}{(\sigma - \Delta\sigma/2)(1 - \gamma)} \quad (4.1)$$

following Scholz *et al.* [1972], where σ is the shear stress at the onset of slip, $\Delta\sigma$ is the stress drop, and γ is the seismic efficiency of radiating the accumulated strain energy as seismic waves. Typical values of μ_s/μ_k range from a little over 1 to about 1.44 [Dieterich, 1974]. "Slip weakening" occurs when the frictional resistance decreases with increasing slip, and there is then accelerating slip prior to instability. Accelerated slip at depth concentrates shear stresses closer to the fault plane. However, there is no means in this model for the fault to regain strength after failure. Rate-dependent friction thus maybe introduced, but this "velocity weakening" is subject to point-wise instability, which does not ensure that an entire fault segment slips in equilibrium during failure [Horowitz and Ruina, 1989]. State-dependent friction laws, based on laboratory studies, appear to yield the behavior most representative of actual faults. Segall [1991] reviews various fault models and instability mechanisms.

Again, we note that local strain monitoring networks which employ both broadband digital seismographs and high-resolution geodetic measurements can address realistic fault models if they can provide constraints on material properties and mechanical behavior of fault zones. The distribution of surface velocity

is a function of distance from the fault, with the strain becoming increasingly nonuniform as the earthquake approaches, suggesting that conversion of line length data to velocities is a better representation of the deformation [Tullis, 1988]. For an earthquake prediction monitoring program, therefore, additional measurements of strain and displacement could be undertaken at depths of about 5 km in **boreholes**, where the slip instability is first pronounced [Tullis, 1988]. Surface velocities lag those at depth, with stress changes at various depths occurring due to changes in frictional slip resistance with depth and thus variations in elastic coupling.

4.2 Preseismic Strain

Recent work on rate- and state-dependent friction **constitutive** relationships [e.g., Tse and Rice, 1986] suggests fairly simple mechanical models of fault behavior, with imperceptible precursive slip but significant **postseismic** slip (the **latter** involving a larger depth range). Two-dimensional models suggest that **pre-seismic** slip rates of the order of 10 to 100 **mm/yr** would have to be resolved in a few days to a month over baselines of a few kilometers in length [Lorenzetti and Tunis, 1989]. Small-scale precursory and long-term **postseismic** strain rates imply that **crustal** deformation measurements must have a resolution of about 10^{-8} **ε** in order to distinguish mechanical properties at depth [e.g., Savage, 1990]. This represents a relative distance measurement accuracy of 1 mm over a 100 km baseline (1 part in 108). However, required accuracies are higher for three-dimensional models.

Deformation immediately prior to an earthquake, which may be used as a short-term precursor, has not been resolved with strain instruments to date. The seismic moment associated with **pre-instability** slip scales with the cube of the radius of the instability nucleation zone [Segall, 1991]. Precursory strains account for only about 0.1 to 1% of the coseismic strain [e.g., Agnew and Wyatt, 1989; Johnston et al., 1990]. The slow, long-period rupture events (Section 4.6) suggested by Beroza and Jordan [1990] also may be associated with accelerating instability.

4.3 Coseismic Strain

Measurements of **coseismic** displacements and corresponding strain perhaps are the most obvious application of geodesy for complementing seismic data and constraining estimates of fault slip at depth. For space-based geodetic networks, the greatest advantage in this regard lies in consistent high-resolution measurements of spatially related strain changes at regional distances and temporally related strain changes before and after rupture.

The coseismic strain change is related directly to the seismic moment, M_0 , which was discussed in Section 2.2. For the root-mean-square (**rms**) of several independent components of strain at one location, or **rms** of any given strain azimuth averaged around a circle of **constant** hypocentral distance, where the strain change $\Delta\epsilon_{rms} < 10^{-7}$, the average spatial distribution is given by

$$\Delta\epsilon_{rms} = 4 \times 10^{-12} M_0/R^3 \quad (4.2)$$

where R is **hypocentral** distance (in meters) [Wyatt, 1988]. This average relationship is substantiated by McGarr et al. [1982] and Shimada et al. [1987]. Using a long-base **strainmeter** at an **epicentral** distance of 97 km from the main shock, Agnew and Wyatt [1989] show no evidence of precursive strain changes associated with the 1987 Superstition Hills, California, earthquake sequence. This is consistent with the results of Lorenzetti and Tullis [1989] for uniformly applied strain (the Superstition Hills earthquake was triggered by a stress change due to the Elmore Ranch earthquake about 12 hr earlier). However, an extensional strain change of 1.5×10^{-9} **ε** (about 10 percent of the coseismic strain change) was recorded in the **first** 5000s after the main event. GPS geodetic measurements of strain accumulation and coseismic offsets associated with the Superstition Hills earthquake are described by Larsen [1990], Larsen et al. [1992] and Larsen and Reilinger [1992],

4.3.1 Triggered Events

Coseismic stress changes related to nearby fault slip, and leading to creep events or secondary earthquakes, are a way of studying fault response and possibly yielding important constraints on the **constitutive** properties of fault zones. *Allen et al. [1972]* and *Fuis [1982]* studied the Superstition Hills fault and **suggest** that triggered slip may be due to a change in the static strain field associated with distant fault rupture, dynamic strain associated with the propagation of seismic waves, creep migration, or a regional strain event manifested both seismically and **aseismically** in different areas. The nature of **aseismic** creep, either **steady-state** or time-variant, and its relation to the earthquake cycle maybe addressed using high-precision geodetic measurements. *McGill et al. [1989]* suggest that triggered slip may occur at any point in the earthquake cycle. The deployment of local to regional geodetic networks spanning several slip-parallel fault segments is an advantage over using a sparse network of creepmeters and **alignment** arrays. Possible resolution of surface deformation associated with triggered slip events [e.g., *Simpson et al., 1988; Williams et al., 1988*] could help constrain the slip (or moment) inversion of the main earthquake. Understanding creep perturbations associated with earthquake rupture also may be important for intermediate-term earthquake prediction [*Simpson et al., 1988*].

4.4 Post-Seismic Strain

Geodetic measurements of **postseismic** deformation, in conjunction with **coseismic** measurements, can contribute significantly toward understanding the rupture propagation process and the relationship with material properties. The effects of time-dependent deformation on geodetic measurements were discussed in Section 3.2.2. We noted that high-resolution (precise and accurate) geodetic measurements of the order of 10^{-8} E are required to image long-term post-seismic deformation and to distinguish between mechanical models of the earthquake source region. Continuously operating (near real-time) geodetic networks (or rapidly deployable networks if previous measurements of an area exist) with fairly high site **densification** are necessary to enable the mapping of surface deformation prior to rupture, including precursory signals, and its subsequent evolution in time. GPS geodesy, in conjunction with broadband seismic instruments, **creepmeters**, **borehole** instruments, and **high-quality strainmeters**, offers the greatest potential return in this regard, given the increasing deployment of continuously operating networks, and the network **densification** made possible by kinematic or rapid static surveys [e.g. *Genrich, 1992*]. We defer further discussion to Section 8.1.

4.5 Fault Creep

The form of creep events, whose amplitude and rise time are related to the geometry (aspect ratio of length and depth) of the slipping patch and fault zone rheology, appears to be slow acceleration for a few minutes, followed immediately by maximum velocity, and slip deceleration for several hours. *Wesson [1988]* gives an excellent account of **fault creep** dynamics. Our interest lies in evaluating whether **space-based geodetic measurements** can **complement creepmeter measurements** by helping address problems that are unresolvable using only small-scale or **small-aperture** networks or alignment arrays. An important **question** is the depth to which surface fault creep extends, particularly since resolution with depth decreases for inversion of surface deformation measurements [*Wesson, 1988*], and because imaging fault motion at greater depths requires surface measurements at greater distances from the fault. Creep at depth may be **related** to thermally activated simple friction. *Savage and Burford [1973]* and *Thatcher [1979]* suggest creep at several kilometers of depth based on **trilateration** and triangulation measurements on baselines more **than** 10 km long. However, several authors cited by *Wesson [1988]* observe that creep events typically are confined near the surface.

The three factors noted by *Wesson [1988]* to cause near-surface fault creep are: (1) stress applied to the fault zone from external sources; (2) stress related to the geometry and distribution of displacement on the fault (the response of the surrounding **elastic** medium to **anelastic** deformation within the fault zone itself); and (3) attributes of the **constitutive** relations describing the frictional behavior on the fault. These parameters, as we have seen, are addressable with space-based geodetic measurements (admittedly, the third factor to a lesser degree). In other words, the potential of local and regional strain monitoring networks is to integrate the deformation from the fault zone out to regional distances, thus helping to assess the spatial

and temporal relationships between these three factors. This, in turn, is important in earthquake prediction models if the creep is treated as a means of stress loading patches of frictional resistance (e.g., asperities) on the fault,

Specification of a depth to the transition zone between the locked (slower slipping) zone at or near the surface and uniform slip below (and above the locked zone if **surficial** creep is introduced) is required to **discretize** a fault plane for creep. This depth is typically the base of the seismogenic zone. The Green's functions for creep are quite simple if **creepmeter** or alignment array data are used, since the system of relevant equations can be partitioned into line-length changes and creep rates. *Harris and Segall [1987]* use this approach to investigate locked zones at depth on the **Parkfield** segment of the San Andreas fault. Geodetic data generally do not have the resolution to distinguish models with a shallow locked zone and smaller rate of slip at depth from deeper locked zone and greater rate of slip at depth [e.g. *Thatcher*, 1979].

4.6 "SLOW" and "Silent" Earthquakes

As the response of long-period seismometers has improved, more evidence has accumulated **concerning** "slow" and "silent" earthquakes. A slow earthquake produces high-frequency body waves associated with high-speed rupture propagation, but the overall duration is long in relation to other events of comparable moment release, and low-frequency excitation is anomalously high [e.g., *Kanamori and Stewart*, 1979]. The 14 January, 1978 Izu-Oshima, Japan, earthquake is discussed by *Sacks et al. [1981]* as a **sequence** of slow events. The June 6, 1960, great Chilean earthquake also is considered a slow event by *Kanamori and Stewart [1979]*. A silent earthquake is a slow earthquake that lacks high-frequency characteristics [e.g. *Bonafede et al.*, 1983]. The rupture velocities of slow and silent earthquakes range of from 1 km/s to 10 m/s [*Beroza and Jordan*, 1990]. Creep events [e.g., *Scholz et al.*, 1969] and strain migration [e.g., *Rundle*, 1978] are associated with rupture velocities of 100 mm/s to 1 m/s, and 1 mm/s to 10 mm/s, respectively [*Beroza and Jordan*, 1990]. Figure 9 summarizes these various characteristic rupture velocities.

The importance of studying earthquakes with low rupture velocities became **apparent** in laboratory work on **constitutive** relations and stable-unstable behavior, such as strain weakening [*Dieterich*, 1979], strain hardening [*Tse and Rice*, 1986], and quasi-static viscoelastic deformation, as discussed earlier. *Beroza and Jordan [1990]* suggest a relationship between slow earthquakes and precursory seismicity that generates the low-frequency radiation prior to high-frequency rupture. The latter is associated with stable aseismic slip prior to unstable stick-slip behavior and possible accelerating slip immediately before rupture [*Dieterich*, 1978]. Low-frequency seismic events can be observed geodetically, depending on the size of the rupture nucleation zone. High-resolution geodetic networks offer an exciting area of research that may benefit from the overlapping bandwidth of seismic observations. Ideally, near-field instrumentation, such as strainmeters and continuous geodetic strain monitoring, is necessary for observing slow precursors; otherwise, an analysis must be based on source time functions determined from long-period teleseismic data.

4.7 Rupture Nucleation Zone

The size of the earthquake nucleation zone is unclear but ranges from several centimeters [*Scholz*, 1988] to several kilometers [*Dobrovolsky et al.*, 1979]. *Ishibashi [1988]* distinguishes between physical precursors to earthquake which are associated with the initiation or progression of rupture and tectonic precursors which are associated with movements of tectonic systems surrounding a rupture preparation zone. He cites the January 14, 1978, Izu-Oshima earthquake (M_s 6.8), and the September 1, 1923 Kanto earthquake (M_s 8.2) as examples of the latter (recall that this Izu-Oshima earthquake was described as a sequence of slow events by *Sacks et al. [1981]*). *Ishibashi [1988]* further states that although deciding whether a precursor (or observed anomalous phenomenon) is physical or tectonic is hampered by poor understanding of fundamental mechanisms for precursory earthquake phenomena, the increased use of space-based continuous plate motion monitoring will help make tectonic precursors more **effective** for practical and quantitative earthquake prediction. The Izu Peninsula in Japan, at the junction of the Pacific and Philippine Sea plates with the Asian plate, is the site of a permanent, continuously operating Global Positioning System geodetic monitoring network [*Shimada et al.*, 1989; 1990; *Yabuki et al.*, 1991; *Shimada and Bock*, 1992] (see Fig. 11, Section 8.1).

5. Simultaneous Inversion of Seismic and Geodetic Data

The first geodetic measurements of the displacement field produced by an earthquake (namely the great 1906 San Francisco earthquake) were obtained by a triangulation network established in the 1880s along the San **Andreas** fault in California [*Hayford and Baldwin, 1907*]. The analysis thereof led *Reid [1910, 1911]* to formulate the elastic rebound theory to explain the accumulation and relaxation of elastic strain before and after fault rupture.

Inversion of geodetic data is inherently non-unique. In this section, we consider whether differences in surface deformation (fault displacement, rupture **velocity**, strain, and **strain** rate) can be measured geodetically. The spatial and temporal distributions of these quantities at the surface are related to the earthquake nucleation process, and to creep acceleration and distribution at depth along the fault plane. The need to constrain the kinematic properties of the fault rupture process using measurements of surface deformation places an upper bound on requisite geodetic resolution. In general, seismic waveform inversion yields the strike, dip, and slip of the **fault**, whereas geodetic deformation data help determine fault length, width, **location**, and the amount of surface **dislocation**, and hence constrain estimates of the earthquake source moment.

Geodetic and seismic data represent static and dynamic displacements, respectively. Spatially, geodetic data constrain the fault geometry and displacement parameters within a few fault widths of the source. Such data can be complemented seismically with regional body waveform data which span the low-frequency response band. Furthermore, displacements can be obtained by integrating near-field strong motion waveforms. This waveform integration can be constrained by the near-field geodetic data. Geodetic data have a long-period response that is not sensitive to the higher frequency characteristics of seismic strong motion records, which are **attributable** to heterogeneous slip distributions.

5.1 Geodetic and Seismic Moments

The displacement $u(x)$ at a point x on the Earth's surface due to slip on a finite fault may be written

$$u(x) = \int_S G(x, \xi) m(\xi) d\xi \quad (5.1)$$

where $m(\xi)$ is the moment density along points on the fault surface S , and $G(x, \xi)$ is the sensitivity kernel or Green's function. $G(x, \xi)$ is a **nonlinear** function of fault parameters (strike, dip, and rake) and relative motions of x and ξ , where ξ is the source location on the fault [*Ward and Barrientos, 1986*]. In order to invert for the slip distribution on the fault, $m(\xi)$ is discretized into N elementary sources (j) and M observations (i),

$$u(x_j) = \sum_{j=1}^N \hat{G}(x_i, \xi_j) s(\xi_j) \quad (5.2)$$

where each unit source consists of an unknown slip. A uniform slip planar model is a simple example of this expression. The Green's function may be specified by the expressions for a uniform strike-slip dislocation in a homogeneous isotropic elastic **halfspace** following *Chinnery [1961]*, *Maruyama [1964]*, and *Press [1965]*.

Ward and Barrientos [1986] describe an iterative gradient technique for solving the typically **underdetermined** ($N > M$) system of equations for variable slip **planar** models. The fault dimension (length along strike, width down dip, and Cartesian (x, y, z) position of an upper fault corner) actually is obtained from the inversion process, either from observational data or from a solution to a simple uniform slip model with the more certain parameters (such as strike) constrained, while dip and slip angles are **sought** parameters given a starting slip dislocation (or starting change in moment). *Barrientos and Ward [1990]* find a discrepancy between the geodetically determined moment from their variable slip model inversion and the **seismically** determined moment. However, this can be minimized by constraining more slip to locations that are not well resolved geodetically, as indicated by the sensitivity kernel for a given fault orientation.

Yoshida and Koketsu [1990] also present a method for simultaneous inversion of strong motion **waveform** data and **triangulation** data to model an earthquake rupture **process**. An example using the 1984

Naganoken-Seibu, Japan ($M = 3 \times 10^{25}$ dyne-cm), earthquake shows that the geodetic (triangulation) data affect peak slip position and slip angle determination. *Saucier et al.* [1992] use a finite element joint **least-squares** inversion of very long baseline **interferometric (VLBI)** and geologic data. Their solution of strain energy minimizing yields estimates of block deformation, motion, and fault slip rates. The fault slip data **are** constrained with seismic, geologic, and geodetic data, while the far-field displacements provide boundary conditions.

The matrix system $Cm = u$ of Eq. (5.2), where the slip and **areal** components are contained within the moments m , may be partitioned into dynamic (seismic) and static (geodetic) elements. The Green's function can be calculated with a generalized reflectivity method [*e.g.*, *Fuchs*, 1968]. *Xie and Yao* [1991] apply this method to determine the rupture process of the July 27, 1976 Tangshan, China, earthquake ($M_s = 7.8$). They point out that long-period **teleseismic** data have a temporal resolution more commensurate with that of geodetic **data**, which sparsely sample the low-frequency properties of the source. Assuming that the static displacement on a fault is related to the total seismic moment associated with each **subfault**, the static moment can be expressed in terms of **teleseismic** moment data. The equations for simultaneous inversion of **teleseismic** waveform data and geodetic data are written in the form

$$W \begin{bmatrix} G^d \\ G^s \end{bmatrix} m = W \begin{bmatrix} u^d \\ u^s \end{bmatrix} \quad (5.3)$$

subject to $Im \geq 0$, where the superscripts refer to dynamic (d) and static (s) data, and the weights W account for differences in data reliability, quality, and resolution [*Xie and Yao*, 1991].

The solution to this system of equations is obtained by a minimum L^2 residual norm, or least squares, method. Use of a generalized inverse approach with singular value decomposition of G has the advantage of indicating which parameters are well determined (resolution) and which data are more important (information) [*Wiggins*, 1972; see also *Aki and Richards*, 1980]. For example, if **teleseismic** data yield a small range of take-off angles, then poor horizontal spatial resolution results. On the other hand, geodetic **data** generally yield much less temporal resolution but may provide higher spatial resolution near the fault.

Simultaneous inversion of dynamic and static displacement data are justified provided the respective moments **are** comparable, or in other words, the slip behavior of the fault is completed within a short rise time. *Xie and Yao* [1991] obtain a larger geodetic moment than that estimated from seismic body wave **data**. Possible explanations are: (1) static data contain long-period contributions outside the body wave **frequency** band; (2) there are contributions from aftershock sequences; and (3) there is aseismic fault creep. Aseismic slip in the period of days to weeks following an earthquake can be an appreciable amount of the total seismic moment, contributing to a larger geodetic moment (for example, see *Prescott et al.*, [1984]). *Smith and Wyss* [1968], however, point out that slip was not observed for 59 days near the epicenter of the 1966 **Parkfield**, California, earthquake, and that it was episodic rather than a smooth decrease in slip rate. Episodic **afterslip** similarly was observed after the 1979 Imperial Valley, California, earthquake [*Cohn et al.*, 1982], and after the 1987 Superstition Hills earthquake [*Bilham*, 1989].

The analysis by *Tajima and Tralli* [1991] (see Section 2.2) indicates a substantial difference between slip estimates derived from cumulative centroid moment data and GPS geodetic slip estimates which concur with the tectonic slip predicted by a recent global plate model. Although seismic slip estimates contain some ambiguity, this discrepancy also can be attributed to a seismic data time window which is small and unrepresentative compared to the geologic time frame, and uncertainties in fault geometries at depth biasing the **seismic** slip estimates. The complementarity of geodetic and seismic measurements is evident.

6. Space-Based Geodetic Techniques

Up to this point, we have **reviewed** the relationships between seismic measurements of ground motions due to an earthquake and corresponding **geodetic** measurements of surface deformation. Various **phenomena** associated with the fault rupture process have been outlined, with emphasis placed on the spatial and temporal characteristics of surface deformation. Many problems in **crustal** deformation modeling which are least understood can benefit most from high-resolution geodetic measurements consisting of dense spatial coverage and sufficiently fine temporal sampling, in anticipation of measuring subtle deformation behavior.

Space-based geodetic measurements also can be used to study a variety of global geophysical parameters given the nature of the data reduction and the need to define a stable coordinate reference frame. These parameters include Earth orientation, such as length-of-day fluctuations in the angular velocity of rotation, and internal Earth structure, such as the distribution of elastic properties, and boundary layer effects resulting from the coupling between the solid mantle and fluid outer core.

In this section we describe briefly the three primary space geodetic techniques — very long baseline interferometry (VLBI), satellite laser ranging (SLR), and measurements with the Global Positioning System (GPS) — and the typical problems addressed by each. Figure 10 schematically illustrates each of these techniques. Results of previous work are presented to show the levels of achieved geodetic resolution to date, the types of problems addressed, and to focus on directions of potential future research.

VLBI, SLR, and GPS are used for geodetic investigations of plate motions, plate boundary zone deformation, and earth orientation. However, for geodetic studies of lithospheric deformation over regions which span a few hundred kilometers or less, GPS is most practical because of lower instrumental costs and higher portability. For areas where the immediate interest is to image the strain distribution pattern associated with a given fault, we will define the relevant zone of deformation to be less than 100 km from the fault plane, typically within only a few fault widths,

Space-based geodesy consists of three-dimensional absolute positioning by simultaneous inversion of range measurements between ground receivers and source transmitters or reflectors (e.g. GPS and SLR, respectively) or by interferometric analysis of radio data (e.g. VLBI). This is fundamentally different from relative line-of-sight measurements of distances in trilateration, angles in triangulation, and variations in local vertical in leveling. A space-based geodetic baseline is simply the vector (chord) between any two network sites, defined with respect to a regional or global (e.g., earth-centered) coordinate reference (often called “fiducial”) frame [see *Blewitt et al.*, 1992]. Over a given baseline, relative changes in such three-dimensional absolute positioning estimates in theory allow self-consistent determinations of plate motions and strain and tilt. Uncertainties in relative motion estimates depend on single measurement accuracy, the interval between measurements, and the time span of total measurements [Coates et al., 1985]. Reference frame errors, or fiducial coordinate uncertainties, can bias baseline estimates and derived strain rates [Larson et al., 1991], as can an order of magnitude difference between horizontal and vertical baseline component errors.

Translational, rotational, and areal dilatational errors must be considered in the analyses of network geodetic measurements. While translation of an entire network has no effect on relative distances between member stations, network rotations particularly can affect determinations of fault-parallel motion, for example, and in certain cases constraints must be adopted to minimize fault-normal motions [e.g., Prescott, 1981; Prescott et al., 1981]. The displacement rates of geodetic stations in a network may be used to estimate the components of the strain rate tensor and a possible rigid body rotation rate. In two-dimensions, a linear system of equations maybe expressed by

$$\begin{bmatrix} \dot{U} \\ \dot{V} \end{bmatrix} = \begin{bmatrix} \dot{\epsilon}_{11} & \dot{\epsilon}_{12} \\ \dot{\epsilon}_{21} & \dot{\epsilon}_{22} \end{bmatrix} \begin{bmatrix} X \\ Y \end{bmatrix} - \begin{bmatrix} 0 & -\dot{\omega} \\ 0 & +\dot{\omega} \end{bmatrix} \begin{bmatrix} X \\ Y \end{bmatrix} \quad (6.1)$$

where U and V are the displacements in the X and Y coordinates, respectively, and Y is parallel to the fault. This may be solved in a least squares sense to obtain the fault normal and parallel strains, the shear strain, and rotation. For example, space-based geodetic measurements may be used to detect regional block rotation observed in paleomagnetic studies and suggested by seismicity patterns [e.g., Nicholson et al., 1986].

Although VLBI, SLR, and GPS geodetic measurements are susceptible to translational and rotational effects, such effects are less likely than in traditional local geodetic techniques because of the global nature of space-based measurements. Inconsistencies in the use of coordinate reference frames may introduce network-wide effects for example, when adjusting network site coordinates by implementing a plate tectonic model and accounting for earth rotation and polar motion. The fiducial approach to GPS data reduction in addition is prone to external errors because of the geodetic ties, and thus dependence, that must be established with VLBI and/or SLR sites in order to provide a requisite coordinate reference frame for estimating geodetic and satellite orbital parameters. In general, the origin, orientation, and time evolution of this origin and orientation with respect to the physical network sites must be well-defined (constrained) to provide a stable reference frame. Unlike VLBI, GPS is sensitive to the dynamical origin of the terrestrial reference frame (the Earth center of mass, or geocenter). However, scale length effects (due to uniform gravitational

and earth model parameters, such as the product of the gravitational constant and Earth mass, GM), which correspond to **areal dilatational** network errors mentioned above, may result in systematic baseline errors and thus require an additional constraint. Many of the **intercomparisons** between these space-based geodetic techniques are aimed at determining coordinate transformation parameter values, understanding differences in the reference frames, assessing which what factors yield error sensitivity, and developing a compatible reference frame [e.g. *Blewitt et al.*, 1992], such as the International Terrestrial Reference Frame (ITRF) [*International Earth Rotation Service, 1991 Annual Report*, IERS Central Bureau, Observatoire de Paris, 1992] using each of these three types of measurements. This effort is necessary to ensure the long-term stability of high-resolution space-based **geodetic** measurements for scientific investigations.

6.1 Very Long Baseline **Interferometry** (VLBI)

Geodesy with very long baseline **interferometry** (VLBI) is based on positioning estimates at radio telescope sites **distributed** on the Earth. Signals are recorded from **extragalactic** radio sources, with observed frequencies centered near 8.3 and 2.3 GHz and sampled to ± 0.3 GHz with 2 MHz frequency windows. The signals are cross-correlated to obtain the difference in group delay (arrival time) and the rate of change of the **interferometric** phase delay (the phases between two telescopes are correlated when both distances to the common radio source are equal). The difference in group delay (t) is proportional to the chord distance L (**baseline** length) between telescopes and the sine of the angle ϕ between the baseline and the radio source ($t = L/c \sin \phi$, where c is the radio wave velocity) [*Clark et al.*, 1987]. Hydrogen maser frequency standards provide precise time-tag information. When many different radio sources are observed, **each** for about 100-400 s over an interval of 24-48 hr, the ensemble of delay and rate measurements can be used to determine the relative positions of the radio telescopes (and the radio sources) with a precision of better than 1 part in 10⁹ of the inter-telescope distances [*Herring et al.*, 1990].

Although VLBI is a highly precise means of measuring distances and earth orientation parameters [e.g., *Herring et al.*, 1986; *Gwinn et al.*, 1986], geodetic applications are regional and global in nature, and can be undertaken between sites only where radio telescopes (or mobile systems) are present. *Clark et al.* [1985] describe the Mark-III VLBI system. Analysis techniques and geodetic parameter modeling and estimation are described by *Herring et al.* [1990] and references therein.

6.2 Satellite Laser Ranging (SLR)

Geodetic measurements with satellite laser ranging (SLR) consist of transmitting very short (1 s) laser pulses to **retroreflectors** mounted on earth-orbiting satellites and measuring the pulse travel time, thus obtaining the distance to the **satell** itc. A series of range measurements with a global network allows determination of satellite orbital parameters and geodetic positions of the ground-based satellite tracking systems. The French geodetic satellite *Satellite* was launched in 1975, and the NASA Laser Geodynamics Satellite (LAGEOS) was launched in 1976, dedicated exclusively to laser ranging for geodynamical applications. *Christodoulidis et al.* [1985] give a description of data analysis for obtaining tectonic plate motions and **geodetic** coordinates [*Smith et al.*, 1985; *Tapley et al.*, 1985]. Lunar laser ranging (LLR) is a similar technique where **retroreflectors** instead have been placed on the surface of the moon [*Dickey and Eubanks*, 1985], and has been used more for long-term studies of earth rotation and earth-moon system parameters [*Langley et al.*, 1981]. Subtle perturbations in satellite orbits are related to mass redistribution within the earth. Laser ranging measurements also have been used to constrain surface loading and postglacial rebound parameters, and to study the effect of inelasticity on long-period earth tides. Scientific results of LAGEOS are presented in a special issue of the *Journal of Geophysical Research* [see *Cohen and Smith*, 1985].

6.3 **Global** Positioning System (GPS)

The types of **crustal** or **lithospheric** motion problems addressable with VLBI and SLR typically are more within the scopes of tectonics and global **plate** motion studies [e.g., *Christodoulidis et al.*, 1985; *Clark et al.*, 1987; *Minster and Jordan*, 1987; *Kroger et al.*, 1987; *Ward*, 1988] than they are within the scope of seismology. Mobile VLBI systems [*Davidson and Trask*, 1985] alleviate this situation to an extent, a recent example being measurements of coseismic displacements of the October 17, 1989, Loma Prieta earthquake ($M_s=7.1$) [*Clark et al.*, 1990] in the southern Santa Cruz Mountains segment of the San

Andreas fault, California. In addition, deployment of VLBI and SLR geodetic systems is costly and often impossible in remote regions or for dense networks.

The Navigation Satellite Timing and Ranging (NAVSTAR) Global Positioning System (GPS) provides the most recent space-based geodetic technique for geophysical investigations, and is perhaps the most exciting because it is applicable to a broad spectrum of problems where seismic measurements can be complemented. High-precision positioning with GPS consists of simultaneous observations of several satellites by a network of ground receivers (any given receiver must observe at least four satellites in order to enable estimates of the three components of position and a receiver clock offset term), GPS satellites eventually will number 24, in 6 orbital planes, with altitudes of about 22,000 km [Green *et al.*, 1989]. GPS signal characteristics are given by *Spilker* [1978] and *Milliken and Zoner* [1978]. Techniques for precise geodetic positioning using GPS are described by *Bossler et al.* [1980] and *Remondi* [1985].

GPS satellites transmit navigational positioning information centered at two L-band frequencies (L1, 1575.42 MHz and L2, 1227.60 MHz). These carrier frequencies are modulated with pseudo-random P-code for precision range measurements (L1 and L2 carrier frequencies are 154 and 120 coherent multiples of 10.23 Mhz, respectively). For a group delay measurement, the received signal is cross-correlated with an internal reference to yield "pseudorange," so termed because of errors in both satellite and receiver clocks. Interferometric differencing techniques may be used to eliminate clock errors common to satellite-receiver pairs [Bock *et al.*, 1986], or the errors may be modeled as polynomial functions or stochastic processes. For a more precise phase delay measurement, also termed integrated Doppler, the total change in phase is measured over several hours and converted to a corresponding range change.

Geodetic estimates of coordinates and earth orientation parameters yield comparable errors using the techniques outlined above. However, the portability and reduced cost of dual-band, multi-channel receivers make GPS the most viable space-based geodetic technique for addressing local and regional deformation, studying plate boundary deformation, fault behavior, and for deployment of dense networks as high-sensitivity strain instruments for fault and volcanic monitoring, establishing an absolute geodetic framework (in conjunction with VLBI) for tide gauge stations in order to monitor eustatic sea level variations and to differentiate such variations from tectonic motions, and for accessing remote areas for studies of tectonic plate interaction, particularly where seismic data may be sparse (for example, in the Antarctic [Shibuya *et al.*, 1990]). We discuss some of these applications in the following sections.

7. Geodetic Constraints on Large-Scale Seismological Problems

Routine analyses of space-based geodetic data involve modeling parameters that are of interest to regional and global seismological problems. In contrast to localized fault monitoring applications, in this section we discuss briefly the use of long baseline measurements for studies of regional deformation and tectonic plate motion, earth orientation, the effects of core-mantle coupling, and the propagation into the atmosphere of waves due to acoustic sources in the solid earth.

7.1 Regional Geodetic Baselines and Tectonic Plate Motion

Geophysical applications of VLBI are reviewed by *Robertson* [1991]. The determination of plate motions from SLR measurements is discussed by *Christodoulidis et al.* [1985]. *Dixon* [1991] reviews the results of several GPS geodetic experiments to date, emphasizing the use of GPS for plate motion studies where, for example, constraints provided by spreading center and transform geometry are poor and slip vectors are insufficient.

Epoch (periodic) measurements of long geodetic baselines (greater than a few hundred kilometers) across tectonic plate boundaries yield the far-field limit of the strains attributable to motion along corresponding fault systems that are driven by the relative plate motion. In fault models, the far-field displacement rates provide the boundary conditions that must be satisfied by stresses originating near the rupture zones [e.g., *Saucier*, 1992]. Constraining regional strain, therefore, is a natural extension of understanding localized strain accumulation on faults and is an important element of understanding boundary zone deformation and propagation of stresses onto continents.

7.2 Subduction Zones

The earthquake mechanism in subduction zones is related, to a certain extent, to the *types* of strain accumulation and release processes discussed previously in Section 3 for strike-slip or transform **plate** boundaries. For example, *Savage [1983b]* assumes an earthquake cycle with locking in the main thrust zone superimposed on steady-state **aseismic** subduction at the plate convergence rate. *Thatcher and Rundle [1984]* include the effects of **asthenospheric** relaxation by imposing normal slip. Measurements of **associated** surface deformation perhaps lend themselves more to regional space-based geodesy given the **areal** extent of potential rupture due to large or great earthquakes, the more complex behavior associated with deep subduction zone earthquakes, and the difficult access to sites of interest (often requiring the occupation of a few remote islands, each of which represents a single point on a tectonic plate in order to provide **trench-crossing** baselines).

Spatial and temporal variations of mechanical strength associated with the stress fields of subduction and outer-rise zones can be obtained from seismic data analyses. Geodetic measurements may contribute to understanding the relationship between **compressional** stress regimes and down-dip tensional stresses related to earthquakes of different depths at **interplate** boundaries [see *Dmowska and Lovison, 1988*]. As GPS networks expand and globally distributed geodetic observatories are established, more data will become available to investigate the mechanical state of the plate boundaries and to determine the stage of an earthquake cycle, including the effects of oblique convergence, variations in slip rates, and thus the potential for a great earthquake.

7.3 Earth Orientation

VLBI, SLR, and LLR (and optical **astrometry**) studies have contributed greatly to studies of Earth rotation and polar motion [e.g., *Dickey and Eubanks, 1985; Dickey et al., 1985*]. Recently, GPS has become an increasingly viable high-resolution technique in this area [e.g. *Lichten et al., 1992; Lindqwister et al., 1992*]. Such studies, for example, include modeling the effects of the Earth's elastic parameters, and accounting for deviations of the core-mantle boundary from hydrostatic equilibrium from analyses of inferred **lateral** variations in lower mantle velocity structure and low-order variations in the geoid [*Richards and Hager, 1984; Hager et al., 1985*]), the kinematic viscosity of the core, and the tidal response of the Earth, **Nutation** theory [e.g., *Wahr, 1981*] provides a means of reducing **astrometric** observations, based on assumptions about properties of the Earth that can be constrained by global seismic data, including body wave, surface wave, and free oscillation data (namely the splitting of normal modes due to the Earth's rotation [*Dahlen, 1968*]), estimating the temporal **Q** of given modes from their spectral widths [*Stein and Geller, 1977*], and determining the effects of a fluid core [*Smith, 1977; Smith and Dahlen, 1981*]. Corrections to the **nutations** series for obliquity and longitude angle are estimated simultaneously with geodetic parameters using a least-squares or **Kalman filter** technique [*Herring et al., 1990*].

Geodetic baseline estimates may be transformed from a crust-fixed to an inertial reference frame by a matrix product that accounts for precession, **nutations**, diurnal spin, and polar motion or Chandler "wobble" [*Herring et al., 1986*]. High-resolution measurements of earth rotation, UT1-UTC, and length-of-day (LOD) fluctuations in the angular velocity of the Earth's rotation can be explained in terms of internal changes in angular momentum associated with the core, **mantle**, and atmosphere (e.g. atmospheric angular momentum) and hydrosphere system (LOD is the negative of the time derivative of the earth orientation parameter UT1, the total rotational phase angle). *Slade and Yoder [1989]* discuss possible excitation of the Chandler wobble by the great 1960 Chilean earthquake. Further discussion of the plausibility of earthquake excitation mechanisms is provided by *Stacey [1977]*, including the effect of **mantle Q** on wobble damping, and by *Chao and Gross [1987]* and *Preisig [1991]*. For example, a greater **anelasticity** (lower **Q** value) results in an amplification of the response due to variations in the shape of the solid Earth (**moment of inertia**) which are associated with solar-lunar tidal effects on great earthquakes.

7.4 Core-Mantle Coupling

In **nutations** theories [*Wahr, 1981; Sasao et al., 1980*], the Earth's mantle and core are coupled by inertial, magnetic, and viscous forces. Inertial forces are the **largest** and arise from **mantle** pressure deflecting the core fluid during **nutations**, and producing a non-zero net torque as the core is flattened. Core flow thus

mentioned in Section 7, and would support the efforts of more regional and local networks distributed throughout the globe. In this section, we address the capabilities of permanent GPS monitoring networks as high-resolution strain instruments on a **local** to regional scale, and we discuss the potential benefits of collocating a global GPS geodetic network with existing global seismographic networks with modern **digital** seismographic instruments.

8.1 Localized Strain Monitoring

Continuously recording GPS monitoring stations [*Shimada et al., 1989; 1990; Yabuki et al., 1991; Lindqwister et al., 1991*] can be deployed in a manner analogous to large-scale **strainmeters**. Figure 11 shows the location of an automated fixed-point GPS network installed in the south **Kanto-Tokai** region surrounding Tokyo, Japan. Changes in the components of a 10 km baseline overlying the **Teishi** undersea volcano are shown in **Fig. 12**. After the peak of the seismic swarm prior to the eruption, a 10 cm change in **north-south** and 8 cm change in east-west baseline components was observed, with an overall baseline length extension of about 10 cm. These are the first continuously operating GPS network results to show correlation of **crustal** deformation with a **seismo-volcanic event**, and are particularly remarkable given the relatively low resolution due to a weak GPS satellite tracking geometry at the time [*Shimada et al., 1990*]. *Okada and Yamamoto [1991]* present a model for this activity by combining various **crustal** movement data with seismic data.

Successful detection of deformation signals, over a given spatial **extent**, is dictated by the spectrum of the deformation in relation to that of the measurement noise. Continuously recording **strainmeters** (and **tiltmeters**) yield resolutions typically better than 10^{-9} ϵ for short-term signals [*Wyatt, 1988*]. In fact, very high sensitivity **borehole strainmeters** have a resolution of 10^{-5} to 10^{-12} , with a 0-10 Hz strain response capable of recording static and dynamic offset., however with an instrument drift rate of about 10^{-7} /yr. Although **strainmeters** have such high sensitivity, errors do increase in time (t) approximately as $t^{1/2}$ because of instrument calibration errors, and therefore **longer** period signatures are harder to resolve. Assuming that measurements are carried out at constant intervals Δt , only deformation signatures greater than $2\Delta t$ are resolvable, corresponding to frequencies below the Nyquist (f_N). The one-sided power spectral density (PSD) can be written

$$P(f) = K f^{-\alpha}, f < (2\Delta t)^{-1} \quad (8.1)$$

[*Agnew, 1987*]. For high-precision laser **strainmeters**, this representation is adequate for frequencies below 10^{-4} Hz, with the frequency fall-off term (α) equal to 2.5 [*Agnew, 1986*].

Strainmeters measure differences in relative distance, whereas GPS geodesy consists deriving strain rates from baseline component changes between measurement epochs which are defined in an absolute **earth-centered** reference frame. Following the idealized approach of *Agnew [1987]*, errors in strain estimates based on differences in absolute positioning are assumed to be **uncorrelated** beyond period t_0 . The PSD is white below the corner frequency f_c (t_0^{-1}), and is scaled by the strain estimate variance σ_ϵ^2 divided by the Nyquist frequency,

$$P_0 = \sigma_\epsilon^2 / f_N \quad (8.2)$$

in accordance with **Parseval's theorem**. Beyond f_c , the PSD falls off at a rate that depends on the noise correlation. The crossover frequency (f_c) between the **strainmeter** and GPS measurement PSDS is determined by equating $P(f)$ in Eq. (8.1) to P_c in Eq. (8.2),

$$t_c = (2\Delta t \sigma_\epsilon^2 / K)^{1/\alpha} \quad (8.3)$$

where t_c is the crossover period (f_c^{-1}). For deformation signals with periods greater than t_c , GPS measurements are preferable due to their smaller relative noise level. These various spectral relationships between **strainmeters** and GPS measurements are illustrated schematically in **Fig. 13**.

8.1.1 Geodetic Measurement Errors

Strain variances obtained from differences in geodetic estimates of short (local) distances L can be expressed in the form

$$\sigma_{\epsilon}^2 = a^2 L^{-2} + b^2 + c^2 L^{-2} (1 - e^{-L/\lambda})^2 \quad (8.4)$$

as suggested by *Dixon [1991]* and shown in **Fig. 14a**. In the case of GPS measurements, the term a is derived from intrinsic receiver noise and set-up errors, while b is related principally to uncertainties in satellite ephemerides. At distances of less than about 100 km, errors associated with estimation of GPS satellite ephemerides are insignificant because they can be different between stations [*Bock et al., 1986*]. A transitional dependence on tropospheric path delay errors is given by the term scaled by c , where λ is the spatial correlation length of tropospheric water vapor throughout the GPS network. If the term c is dropped in eq. (8.4), corresponding to regional rather than **local** measurements, typical estimated values for a are 5 mm, and 3×10^{-9} for b for horizontal component VLBI baseline determinations [*Clark et al., 1987*], and ranging from 3 to 8 mm for a and $1\text{--}2 \times 10^{-8}$ for b in regional GPS measurements [*Dixon et al., 1991a,b*]. Both VLBI and GPS yield an order of magnitude improvement over traditional geodetic techniques, such as using **Geodolites**, where the baseline length-dependent term is 2×10^{-7} [e.g., *Savage and Prescott, 1973*]. However, over baselines ranging from 10 to 50 km, *Davis et al. [1989]* find no significant differences between **Geodolite** and GPS measurements, with an accuracy of 1-2 mm/yr in slip rate estimates.

Differential ionospheric effects may be another significant error source in local GPS networks. Although dual-band measurements can be used to reduce dispersive ionospheric path delays by forming a linear combination of the GPS observable [*Bock et al., 1986; Blewitt, 1989*], this “ionosphere-free” **combination** amplifies dispersive effects, including signal **multipath** (scattering); hence it may be preferable to analyze dual-band data **separately**. Otherwise, there is a complicating factor in the error term a of Eq. (8.4). The tradeoff between noise amplification and elimination of length-dependent errors due to orbits, **tropospheric** path delays, residual ionospheric effects, and the distance between GPS stations determine the effective precision of the geodetic measurements.

Baseline *precision* is defined by the scatter of individual estimates about a mean weighted by the formal errors of each estimate. The terms in Eq. (8A) can be estimated by regression of these “repeatabilities” on baseline length, assuming that the scatter is comparable to the error of any given estimate. Long-term errors such as monument instability, which also are significant in **strainmeter** measurements, may dominate over periods of **several years**, and therefore to a lesser degree affect the ability to resolve baseline changes over smaller time spans. Fiducial, or global satellite tracking network, station coordinate uncertainties may bias estimates systematically, thus affecting *accuracy* [e.g., *Davis et al., 1989; Tralli and Lichten, 1990*] and also *precision* if the network is not **repeated** exactly during each observation session.

Based on experiments over baselines of a few kilometers to hundreds of kilometers in length [e.g., *Tralli et al., 1988; Blewitt, 1989; Dong and Bock, 1989; Davis et al., 1989; Dixon et al., 1991a,b; Larson and Agnew, 1991; Shimada and Bock, 1992*], GPS precision in horizontal components has been demonstrated to be at a level of 0.1 to 1.0 cm for baselines up to 100 km. *Genrich and Bock [1992]* present the results of a 250 m GPS alignment array near **Parkfield**, California, with a **submillimeter** static measurement precision and millimeter-level kinematic precision. These error levels can be modeled using Eq. (8.4) as a 0.1 cm constant error for receiver noise, 3 parts in 10^8 length-dependent error, and an asymptotic contribution of 0.5 to 1 cm due to tropospheric path delays [e.g., *Davis et al., 1985; Tralli and Lichten, 1990*] with λ of 50 to 100 km (**Fig. 14b**). Vertical baseline component errors are higher and related directly to tropospheric path delay **errors** provided carrier phase cycle ambiguities are resolved [*Tralli et al., 1988*].

8.1.2 Comparison with **Strainmeter** Measurements

The tradeoff between sampling interval (Δt) and strain measurement precision (σ_{ϵ}) is denoted by Eq. (8.3). A measurement span of n (> 1) days decreases the geodetic estimate error by averaging, but reduces the resolution of higher-frequency signals. However, with geodetic sampling intervals of less than 1 day, the GPS uncertainties increase due to decreased satellite observation time and thus **less** data redundancy for parameter estimation. Figure 14b shows that for a 20 km baseline, daily GPS sampling with an **asymptotic**

total tropospheric path delay error of 0.5 cm yields a comparable frequency crossover to half-day sampling with a 1 cm tropospheric error. Decreasing the geodetic sampling interval of the **GPS** measurements improves their utility relative to **strainmeters**. In general, at longer periods the GPS noise has a lower PSD, indicating longer-term stability. A smaller tropospheric correlation length increases the GPS error (Fig. 14a) and thus increases the crossover time (Fig. 14b).

Electronic distance measuring (**EDM**) has a functionally similar noise PSD to that of GPS measurements [Agnew, 1986]. *Davis et al.* [1989] show excellent agreement between **Geodolite** and GPS measurements over distances of about 10 to 50 km. *Agnew [1986]* shows EDM and **strainmeter** crossover times assuming a constant error of 0.7 mm and a length-dependent error of 1.2 parts in 10^7 . However, the advantage of GPS measurements is that smaller error levels can be maintained over distances in excess of a hundred kilometers, thus enabling consistent localized fault monitoring and measurements of possibly related strain changes at greater distances [e.g., *Simpson et al., 1988*] simultaneously in three components, although this is more difficult to achieve in practice.

Temporal PSD models of noise in GPS and high-quality **strainmeter** measurements of **crustal** deformation suggest that GPS may be preferable for short-term signals in under 6 months of continuous observations over distances up to 100 km, assuming a GPS geodetic precision of 0.1 to 1.0 cm in horizontal baseline components. Although it is possible to obtain GPS geodetic estimates every few minutes, given proper network design and satellite geometry, tropospheric path delay errors may become highly correlated and **periodic** errors attributed to **signal multipath** may not be reduced by averaging. These errors may obscure short-period strain signals [Tralli, 1991].

Strainmeter and GPS measurements are complementary due to the differences in temporal noise spectra and the range of distances over which these measurements can be made. Realistic **crustal** deformation modeling which accounts for strain accumulation and fault dynamics requires near-field strain measurements, high-precision **local** and regional geodetic data, and broadband seismic data. These measurements enable the investigation of the entire range of spatial and temporal deformation scales. The spectral models described here will be tested in the near future with data from continuous GPS monitoring arrays to determine when and where GPS measurements are useful in this regard.

8.2 Collocation with Seismographic Networks

In the previous sections of this paper, we discussed the theoretical relationships between measurements of surface deformation, seismic source characterization, and earth structure. The questions we address now are: What can be gained from a seismological or tectonic viewpoint by establishing a global network of geodetic (**GPS**) stations, and what are the scientific advantages of collocation with broadband seismographic networks such as the Incorporated Research Institutions for Seismology (IRIS) Global Seismographic Network?

High-resolution global geodetic network measurements overlap the bandwidth of long-period seismic data. GPS stations operating with sampling rates from 1 s to a few minutes, and collocated with broadband seismographic stations covering a period range of 0.1 to a few hundred seconds, enable ground motion monitoring in the frequency band of 0 to 10 Hz (the low-frequency limit being the length of time the GPS network is operational). Nonetheless, geodetic baselines from such a station would have to be short, or of sufficiently high resolution, to allow the detection of a net deformation (integrated along a given baseline) for comparison with long-period seismic waveforms. In other words, even if a geodetic site is located near the earthquake epicenter, the deformation signatures will be obscured in any baseline solutions that exceed a few fault widths in length unless a dense and smaller-aperture auxiliary network of geodetic receivers is deployed.

The advantages of a global geodetic network are more pragmatic in nature: (1) reference station positions would be established to support dense networks in the event of a major earthquake, either as GPS fiducial stations for periodic measurements or references for rapid static or kinematic surveys near the rupture area; (2) geodetic measurements would be made continuously in the event of an earthquake such that **preseismic**, **coseismic**, and **postseismic** data would be available, while interseismic slip rates could be determined over a long span of observations between events; (3) increased precision of earth orientation **parameters** and long baseline estimates for global plate motion modeling would result from improved GPS satellite tracking and the development of a stable coordinate reference frame such as the ITRF [e.g. *Blewitt*

et al., 1992], as discussed previously in section 6. In addition, the telecommunications and mass storage capabilities of various collocated data type networks could be shared.

A globally distributed network of about 200 high-precision GPS stations would contribute to improvements of global plate tectonic models such as NUVEL-1 [DeMets *et al.*, 1990], which is the most advanced model to date and useful for providing the driving force boundary conditions on regional deformation models. Constraints on mantle viscosity and lateral variations in elastic parameters may be improved given smaller uncertainties on vertical motions for analyses of surface loading, postglacial rebound and asthenospheric relaxation. On the other hand, such a global geodetic network overall may do little to improve the understanding of near-field fault behavior, since constraints on realistic rheological models and source parameters are provided only by spatially and temporally high-resolution near-field measurements. From the standpoint of earthquake seismology, there is greater expectation from concentrated geodetic efforts that focus on monitoring specific seismic and volcanic zones of recognized hazard potential, including areas of complex plate convergence such as subduction and continental collision zones, than from global networks with large inter-station spacing. Several institutions have begun the deployment of regional broadband digital seismographic networks which are collocated with GPS receivers. A global geodetic network simply provides an accurate framework for further geodetic densifications which should be pursued in areas where complimentary seismic and strain instrumentation are operational. The various approaches for the simultaneous inversion of seismic and geodetic data then could be applied to investigate seismic source properties and deformation processes.

9. Conclusions

High-resolution geodetic data obtained with space-based techniques such as VLBI, SLR, and GPS can contribute to the understanding of seismic sources, mechanical models of fault behavior, the partitioning of aseismic creep and seismic slip, the depth distribution of fault slip, the interaction of member faults within a regional fault system, the relationship between fault dynamics and plate boundary deformation, the accumulation and release of tectonic stress, the global interaction of tectonic plates, internal earth structure such as viscosity and elasticity, and earth orientation parameters related to mass distribution. The advantage of space-based geodesy lies in the ability to obtain measurements with a precision of at least 1 part in 10^8 of baseline length over local to regional distances, with comparable accuracy ensured by the long-term stability of the measurements in a robust, globally established, and stable reference frame.

In this paper, we have reviewed the fundamental relationships between a seismic source and the resulting surface deformation, and methods for inverting geodetic and seismic data simultaneously through the characterization of static and kinematic displacements, respectively. Geodetic measurements undertaken at all phases of an earthquake cycle can be incorporated in earthquake source parameterizations, geometrical fault models, and rheological models of fault zone behavior consistent with laboratory studies of rock samples, in order to characterize the strain accumulation and release process in the seismic source region. Regional geodetic measurements may provide constraints on the response of faults to stress loading over distances of several fault widths. The interrelationships between earthquake source, fault, and medium properties may yield new insights into the problem of earthquake prediction, in part allowing or giving direction to the imaging of precursory surface deformation signals that otherwise may be aliased spatially or temporally by traditional geodetic and strain measuring techniques. We also have discussed the response and resolution of the geodetic data required to gain in the understanding of crustal deformation at the various phases of the earthquake cycle. The mechanical conditions of plate boundary deformation are related to the interactive behavior of the individual faults that manifest the boundary itself. Comprehensive modeling of the deformation requires the integration of local and regional measurements of overlapping response to develop dynamic and kinematic models of crustal or lithospheric deformation.

The similarity and complementarity of the deformation measurement response of seismological and space-based geodetic measurements make their combined use innovative for geophysical research. Seismological problems that can be constrained with high-resolution geodetic data include not only large-scale pursuits, such as the nature of the Earth's interior and the effect on orientation and rotation, but also practical applications such as the real-time imaging of surface deformation for active fault and volcanic eruption monitoring, and eventually for hazard mitigation. This potential of seismic and geodetic data is being recognized. In such a manner, seismology and space-based geodesy can benefit mutually by recognizing the

measurement limitations and requirements imposed by each other for addressing geophysical problems. Thus, scientific results that exploit the broader measurement response will be possible, yielding better constraints, smaller uncertainties, and improved models.

Acknowledgments

We thank Y. Bock for reviewing the manuscript, and Y. Okada and R. Dmowska for useful comments. This work was supported by the Geodynamic Program, Jet Propulsion Laboratory, California Institute of Technology, under contract with the National Aeronautics and Space Administration, and by the Institute for Geophysics, The University of Texas at Austin, under NASA grant NAG 5-1041. Contribution No. 898 of the Institute for Geophysics at the University of Texas at Austin.

REFERENCES

- Aki, K., (1966). Generation and propagation of G waves from Niigata earthquake of June 16, 1964, *Bull. earthquake Res. Inst., Tokyo Univ.*, 44, 23-88.
- Aki, K. and P. G. Richards (1980). *Quantitative Seismology*, W. H. Freeman and Co., San Francisco, 932 pp.
- Agnew, D. C., (1986). Strainmeters and tiltmeters, *Rev. Geophys.*, 24,579-624.
- Agnew, D. C., (1987). On noise levels in deformation measurements: Comparison in the frequency domain, Proc. Workshop XXXVH Physical and observational Basis for Intermediate-term Earthquake Prediction, Vol. II, U.S. Geol. Survey Open-file report 87-591,
- Agnew, D. C., and F. K. Wyatt, (1989). The 1987 Superstition Hills earthquake sequence: strains and tilts at Pinon Flat Observatory, *Bull. Seism. Soc. Am.*, 79, 480-492.
- Allen C. R., M. Wyss, J. N. Brune, A. Granz, and R. Wallace, (1972). Displacements on the Imperial, Superstition Hills, and San Andreas faults triggered by the Borrego Mountain earthquake, in *The Borrego Mountain Earthquake*, U.S. Geol. Surv. Professional Paper 787,87-104.
- Austen, J., S. Franke, and C. Liu, (1988). Ionospheric imaging using computerized tomography, *Radio Science*, 23,299-307.
- Barrientos, S. E., and S. N. Ward, (1990). The 1960 Chile earthquake: inversion for slip distribution from surface deformation, *Geophys. J. Int.*, 103, 589-598.
- Bataille, K., and S. M. Flatte', (1988). Inhomogeneities near the core-mantle boundary inferred from short-period scattered PKP waves recorded at the Global Digital Seismographic Network, *J. Geophys. Res.*, 93, 15,057-15,064.
- Beroza, G. C., and T. H. Jordan, (1990). Searching for slow and silent earthquakes using free oscillations, *J. Geophys. Res.*, 95, 2485-2510.
- Bilham, R., (1989). Surface slip subsequent to the 24 November 1987 Superstition Hills, California, earthquake monitored by digital creepmeters, *Bull. Seism. Soc. Am.*, 79,424-450.
- Blewitt, G., (1989). Carrier phase ambiguity resolution for the Global Positioning System applied to geodetic baselines up to 2000 km, *J. Geophys. Res.*, 94, 10,187-10,203.
- Blewitt, G., M. B. Heflin, F. H. Webb, U. J. Lindqwister, and R. P. Malla (1992). Global coordinates with centimeter accuracy in the International Terrestrial Reference Frame using GPS, *Geophys. Res. Lett.*, 19, 853-856.
- Bock, Y., S. A. Gourevitch, C. C. Counselman 111, R. W. King, and R. L. Abbot, (1986). Interferometric analysis of GPS phase observations, *Manuscrip. Geod.*, 11,282-288.
- Bonafede, M., E. Boschi, and M. Dragoni, (1983). Viscoelastic stress relaxation on deep fault sections as a possible source of very long period elastic waves, *J. Geophys. Res.*, 88,2251-2260.
- Bou, M. H. P., and D. S. Dean (1973). Stress diffusion from plate boundaries, *Nature*, 243,339-341.
- Bossier, J. D., C. C. Goad, and P. L. Bender (1980). Using the Global Positioning System (GPS) for geodetic positioning, *Bull. Geod.*, 54,553-564.
- Brune, J. N., (1968). Seismic moment, seismicity, and rate of slip along major fault zones, *J. Geophys. Res.*, 73, 777-784.
- Chao, B. F., and R. S. Gross, (1987). Changes in Earth's rotation and gravity by earthquakes, *Geophys. J. R. Astr. Soc.*, 91, 569-596.

- Chinnery, M. A., (1961). The deformation of the ground around surface faults, *Bull. Seism. Soc. Am.*, 51, 335-372.
- Christodoulidis, D. C., D. E. Smith, R. Kolenkiewicz, S. M. Klosko, S. M. Torrence, and P. J. Dunn (1985). Observing tectonic plate motions and deformations from satellite laser ranging, *J. Geophys. Res.*, 90, 9249-9263.
- Clark, T. A., B. E. Corey, J. L. Davis, G. Elgered, T. A. Herring, H. F. Hinteregger, C. A. Knight, J. L. Levine, G. Lundqvist, C. Ma, E. F. Nesman, R. B. Phillips, A. E. E. Rogers, B. O. Ronnang, J. W. Ryan, B. R. Schupler, D. B. Shaffer, I. I. Shapiro, N. R. Vandenberg, J. C. Webber, and A. R. Whitney (1985). Precision geodesy using the Mark-III very long baseline interferometer system, *IEEE Trans. Geosci. Remote Sens.*, GE-23, 438-449.
- Clark, T. A., D. Gordon, W. E. Himwich, C. Ma, A. Mallama, and J. W. Ryan (1987). Determination of relative site motions in the western United States using Mark 111 VLBI, *J. Geophys. Res.*, 92, 12,741-12,750.
- Clark, T. A., C. Ma, J. M. Sauber, J. W. Ryan, D. Gordon, D. B. Shaffer, D. S. Caprette, and N. R. Vandenberg (1990). Geodetic measurement of deformation in the Loma Prieta, California earthquake with very long baseline interferometry, *Geophys. Res. Lett.*, 17, 1215-1218.
- Coates, R. J., H. Frey, G. D. Mead, and J. M. Bosworth (1985). Space age geodesy: The NASA Crustal Dynamics Project, *IEEE Trans. Geosci. Rem. Sens.*, GE-23, 360-368.
- Cohen, S. C. (1982). A multilayer model of time dependent deformation following an earthquake on a strike-slip fault, *J. Geophys. Res.*, 87, 5409-5421.
- Cohen, S. C., and D. E. Smith (1985). LAGEOS scientific results: Introduction, *J. Geophys. Res.*, 90, 9217-9220.
- Cohn, S. N., C. R. Allen, R. Gilman, and N. R. Gouly (1982). Preearthquake and postearthquake creep on the Imperial Fault and Brawley seismic zone, in *The Imperial Valley earthquake of Oct 151979, U. S. Geol. Surv. Profess. Paper 1254*, 183-191.
- Dahlen, F. A. (1968). The normal models of a rotating elliptical Earth, *Geophys. J. R. Astron. Soc.*, 16, 329-467.
- Davidson, J. M., and D. W. Trask (1985). Utilization of mobile VLBI for geodetic measurements, *IEEE Trans. Geosci. Rem. Sens.*, GE-23, 426-437.
- Davies, K., and D. M. Baker (1965). Ionospheric effects observed around the time of the Alaskan earthquake of March 28, 1964, *J. Geophys. Res.*, 70, 2251-2253.
- Davis, J. L., T. A. Herring, I. I. Shapiro, A. E. E. Rogers, and G. Elgered (1985). Geodesy by radio interferometry: Effects of atmospheric modeling errors on estimates of baseline length, *Radio Sci.*, 20, 1593-1607.
- Davis, J. L., W. H. Prescott, J. L. Svarc, and K. J. Wendt (1989). Assessment of Global Positioning System measurements for studies of crustal deformation, *J. Geophys. Res.*, 94, 13,635-13,650.
- de Hoop, A. T. (1958). Representation theorems for the displacement in an elastic solid and their application to elastodynamics diffraction theory, Thesis, Technische Hogeschool, Delft.
- DeMets, C., R. G. Gordon, D. F. Argus, and S. A. Stein (1990). Current plate motions, *Geophys. J. Int.*, 101, 425-478.
- Dickey, J. O., and T. M. Eubanks (1985). Earth rotation and polar motion: Measurements and implications, *IEEE Trans. Geosci. Rem. Sens.*, GE-23, 373-384.
- Dickey, J. O., XX Newhall, and J. G. Williams (1985). Earth orientation data from lunar laser ranging and an error analysis of polar motion services, *J. Geophys. Res.*, 90, 9353-9362.
- Dieterich, J. H. (1974). Earthquake mechanisms and modeling, *Annu. Rev. Earth Planet. Sci.*, 2, 275-301.
- Dieterich, J. H. (1978). Time-dependent friction and the mechanics of stick-slip, *Pure Appl. Geophys.*, 116, 790-806.
- Dieterich, J. H. (1979). Modeling of rock friction, 1, Experimental results and constitutive equations, *J. Geophys. Res.*, 84, 2161-2168.
- Dixon, T. H., G. M. Gonzalez, S. M. Lichten, and E. G. Katsigris (1991a). First epoch geodetic measurements with the Global Positioning System across the northern Caribbean plate boundary zone, *J. Geophys. Res.*, 96, 2397-2415.
- Dixon, T. H., G. Gonzalez, S. M. Lichten, D. M. Tralli, G. Ness, and J. P. Dauphin (1991 b). Preliminary determination of Pacific-North America relative motion in the southern Gulf of California with the Global Positioning System, *Geophys. Res. Lett.*, 18, 861-864.

- Dixon, T. H. (1991). An introduction to the Global Positioning System and some geological applications, *Rev. Geophys.*, 28, 249-276.
- Dmowska, R., and L. C. Lovison (1988). Intermediate-term seismic precursors for some coupled subduction zones, *PA GEOPH.*, 126, 643-664.
- Dobrovolsky, I. P., S. I. Zubkhov, and V. I. Miachkin (1979). Estimation of the size of earthquake preparation zones, *Pure Appl. Geophys.*, 117, 1025-1044.
- Dong, D. and Y. and Bock (1988). Global Positioning System network analysis with phase ambiguity resolution applied to crustal deformation studies in California, *J. Geophys. Res.*, 94, 3949-3966.
- Elsasser, W. M. (1969). Convection and stress propagation in the upper mantle, in *The Application of Modern Physics to the earth and Planetary Interiors*, ed. S. K. Runcorn, pp. 223-246, Wiley-Interscience, New York.
- Eshelby, J. D. (1957) The determination of the elastic field of an ellipsoid inclusion, and related problems. *Proc. Royal Soc. of London*, A241, 376-396.
- Fuchs, K. (1968). The reflection of spherical waves from transition zones with arbitrary depth-dependent elastic moduli and density, *J. Phys. Earth*, 16, 27-41.
- Fuis, G. S. (1982). Displacement on the Superstition Hills fault triggered by the earthquake, in the Imperial Valley Earthquake of October 15, 1979, *U.S. Geol. Surv. Professional Paper 1254*, 145-154.
- Genrich, J. F. (1992). Geophysical applications of GPS kinematic techniques, Ph.D. thesis, Scripps Inst. Oceanography, Univ. Calif., San Diego, 194 pp.
- Genrich, J. F., and Y. Bock (1992). Rapid resolution of crustal motion with short-range GPS, *J. Geophys. Res.*, submitted.
- Green, G. B., P. D. Massatt, and N. W. Rhodus (1989), The GPS twenty-one primary satellite constellation, *Navigation*, 36, 9-24.
- Gwinn, C. R., T. A. Herring, and I. I. Shapiro (1986). Geodesy by radio interferometry: Studies of the forced nutations of the Earth, 2. Interpretation, *J. Geophys. Res.*, 91, 4755-4765.
- Hager, B. H., R. W. Clayton, M. A. Richards, R. P. Comer, and A. M. Dziewonski (1985). Lower mantle heterogeneity, dynamic topography and the geoid, *Nature*, 313, 541-545.
- Harris, R. A., and P. Segall (1987). Detection of a locked zone at depth on the Parkfield, California, segment of the San Andreas fault, *J. Geophys. Res.*, 92, 7945-7962.
- Haskel, N. (1964). Total energy and energy spectral density of elastic wave radiation from propagating faults, *Bull. Seism. Soc. Am.*, 54, 1811-1841.
- Haskel, N. (1969). Elastic displacements in the near-field of a propagating fault, *Bull. Seism. Soc. Am.*, 59, 865-908.
- Hayford, J. F., and A. L. Baldwin, The earth movements in the California earthquake of 1906, The California Earthquake of April 18, 1906: Report of the State Earthquake Investigation Commission, Rep. 1, pp. 114-145, Carnegie Institution of Washington, Washington, D. C., 1907.
- Herring, T. A., C. R. Gwinn, and I. I. Shapiro (1986). Geodesy by radio interferometry: Studies of the forced nutations of the Earth, 1. Data Analysis, *J. Geophys. Res.*, 91, 4745-4754.
- Herring, T. A., J. L. Davis, and I. I. Shapiro (1990). Geodesy by radio interferometry: The application of Kalman filtering to the analysis of very long baseline interferometry data, *J. Geophys. Res.*, 95, 12,561-12,581.
- Hide, R., and K. Horai (1968), On the topography of the core-mantle interface, *Phys. Earth Planet. Inter.*, 1, 305-308.
- Horowitz, F. G., and A. Ruins' (1989), Slip patterns in a spatially homogeneous fault model, *J. Geophys. Res.*, 94, 10,279-10,298.
- International Global Network of Fiducial Stations (1991). Panel on Global Network of Fiducial Sites, National Academy Press, Washington DC.
- Ishibashi, K. (1988). Two categories of earthquake precursors, physical and tectonic, and their roles in intermediate-term earthquake prediction, *Pageoph.*, 126, 687-700.
- Johnston, M. J. S., A. T. Linde, and M. T. Gladwin (1990). Near-field high resolution strain measurements prior to the October 18, 1989, Loma Prieta Ms 7.1 earthquake, *Geophys. Res. Lett.*, 17, 1777-1780.
- Kanamori, H., and D. L. Anderson (1975). Theoretical basis of some empirical relations in seismology, *Bull. Seism. Soc. Am.*, 65, 1073-1095.
- Kanamori, H., and G. S. Stewart (1979). A slow earthquake, *Phys. Earth Planet. Inter.*, 18, 167-175.

- Keilis-Borok, V. (1959). On estimation of the displacement in an earthquake source and of source dimensions, *Ann. Geofis. (Rome)*, 12, 205-214.
- Kikuchi, M., and H. Kanamori (1982). Inversion of complex body waves, *Bull. Seism. Soc. Am.*, 72, 491-506.
- Kikuchi, M. and H. Kanamori, (1986), Inversion of complex body waves - II, *Phys. Earth Planer. Int.*, 43, 205-222.
- Kikuchi, M. and H. Kanamori, (1991). Inversion of complex body waves - III, *Bull. Seism. Soc. Am.*, 81, 2335-2350.
- Knopoff, L. (1958). Energy release in earthquakes, *Geophys. J.*, 1, 44-52.
- King, G. C. P., R. S. Stein, and J. B. Rundle (1988), The growth of geological structures by repeated earthquakes, 1. Conceptual framework, *J. Geophys. Res.*, 93, 13,307-13,318.
- Kroger, P. M., G. A. Lyzenga, K. S. Wallace, and J. M. Davidson (1987). Tectonic motion in the western United States inferred from very long baseline interferometry measurements, 1980-1986, *J. Geophys. Res.*, 92, 14,151-14,164.
- Langley, R. B., R. W. King, and L. I. Shapiro (1981). Earth rotation from lunar laser ranging, *J. Geophys. Res.*, 86, 11,913-11,918.
- Larsen, S., (1990). Global Positioning System measurements of deformation in southern California, Ph.D. thesis, Calif. Inst. of Technology, 351 pp.
- Larsen, S., and Reilinger (1992). Global Positioning System measurements of strain accumulation across the Imperial Valley, California 1986-1989, *J. Geophys. Res.*, 97, 8865-8876.
- Larsen, S., R. Reilinger, H. Neugebauer, and W. Strange (1992). Global Positioning System measurements of deformations associated with the 1987 Superstition Hills earthquake: evidence for conjugate faulting, *J. Geophys. Res.*, 97, 4885-4902.
- Larson, K. M. and D. C. Agnew (1991). Application of the Global Positioning System to crustal deformation measurement 1. Precision and accuracy, *J. Geophys. Res.*, 96, 16,547-16,565.
- Li, V. C., and J. R. Rice (1987). Crustal deformation in great California earthquake cycles, *J. Geophys. Res.*, 92, 11,533-11,551.
- Lichten, S. M., S. L. Marcus, and J. O. Dickey (1992). Sub-daily resolution of Earth rotation variations with Global Positioning System measurements, *Geophys. Res. Lett.*, 19, 537-540.
- Lindqwister, U. J., J. F. Zumberge, F. H. Webb, and G. Blewitt (1991). Few millimeter precision for baselines in the California Permanent GPS Geodetic Array, *Geophys. Res. Lett.*, 18, 1135-1138.
- Lindqwister, U. J., A. P. Freedman, and G. Blewitt (1992). Daily estimates of the Earth's pole position with the Global Positioning System, *Geophys. Res. Lett.*, 19, 845-848.
- Lorenzetti, E., and T. E. Tunis (1989). Geodetic predictions of a strike-slip fault model: Implications for intermediate- and short-term earthquake prediction, *J. Geophys. Res.*, 94, 12,343-12,361.
- Mahrer, K. D., and A. Nur (1979). Strike slip faulting in a downward varying crust, *J. Geophys. Res.*, 84, 2296-2302.
- Maruyama, T. (1964). Statical elastic dislocations in an infinite and semi-infinite medium, *Bull. Earthquake Res. Inst. Univ. Tokyo*, 42, 289-368.
- Mavko, G. M. (1981). Mechanics of motion on major faults, *Annu. Rev. Earth Planet. Sci.*, 9, 81-112.
- McGarr, A., I. S. Sacks, A. T. Linde, S. M. Spottiswoode, and R. W. E. Green (1982). Cosismic and other short-term strain changes recorded with Sacks-Evertson strainmeters in a deep mine, South Africa, *Geophys. J. R. Astron. Soc.*, 70, 717-740.
- McGill, S. F., C. R. Allen, K. W. Hudnut, D. C. Johnson, W. F. Miller, and K. E. Sieh (1989). Slip on the Superstition Hills fault and on nearby faults associated with the 24 November 1987 Elmore Ranch and Superstition Hills earthquakes, southern California, *Bull. Seism. Soc. Am.*, 79, 362-375.
- Milliken, R. J., and C. J. Zoller (1978). Principle of operation of NAVSTAR and system characteristics, *Navigation*, 25, 201-210.
- Minster, J. B., and T. H. Jordan (1987). Vector constraints on western U. S. deformation from space geodesy, neotectonics, and plate motions, *J. Geophys. Res.*, 92, 4798-4804.
- Najita, K., and P. C. Yuen (1979). Long-period oceanic Rayleigh wave group velocity dispersion curve from HF Doppler sounding of the ionosphere, *J. Geophys. Res.*, 84, 1253-1260.
- Nicholson, C., L. Seeber, P. Williams, and L. R. Sykes (1986). Seismicity and fault kinematics through the eastern Transverse Ranges, California: Block rotation, strike-slip faulting, and low-angle thrusts, *J. Geophys. Res.*, 91, 4891-4908.

- Nur, A., and G. **Mavko** (1974). PostSeismic **viscoelastic** rebound, *Science*, 183,204-206.
- Okada** , Y. and E. **Yamamoto** (1991). A model for the 1989 **seismo-volcanic** activity off **Ito**, Central Japan, derived from **crustal** movement data, *J. Phys. Earth*, 39,177-195.
- Prescott, W. H. (1981). The determination of displacement fields from geodetic data along a strike slip fault, *Journ Geophys. Res.*, 86,6067-6072.
- Prescott, W. H., M. Lisowski, and J. C. Savage (1981). Geodetic measurements of **crustal** deformation on the San Andreas, Hayward, and **Calaveras** faults near San Francisco, California, *J. Geophys. Res.*, 86, 10,853-10,869.
- Prescott, W. H., N. E. King, and G. **Guohua** (1984). Preseismic, **coseismic**, and postseismic deformation associated with the 1984 Morgan Hill, **Calif.** earthquake, *Spec. Publ. Calif. Div. Mines Geol.*, 68, 137-148.
- Press, F. (1965). Displacements, strains, and tilts at **teleseismic** distances, *J. Geophys. Res.*, 70, 2395-2412.
- Preisig, J. R. (1991). Polar motion, atmospheric angular momentum and earthquakes - correlations and significance, *Geophys. J. Int.*, 108, 161-178.
- Reid, H. F. (1910). The mechanics of the earthquake, The California Earthquake of April 18, 1906: Report of the State Earthquake Investigation Commission, Rep. 2, **Publ.** 87, 192 pp., Carnegie Institution of Washington, Washington, D. C..
- Reid, H. F. (1911). The elastic-rebound theory of earthquakes, *Univ. Calif. Publ. Geol. Sci.*, 6,413-444.
- Remondi, B. W. (1985). Global Positioning System carrier phase: Description and use, *Bull. Geod.*, 59, 361-377.
- Richards, M. A. and B. H. Hager (1984). **Geoid** anomalies in a dynamic earth, *J. Geophys. Res.*, 89,5987-6002.
- Roberts, D. S., (1991). Geophysical applications of very-long baseline interferometry, *Rev. Mod. Phys.*, 63, 899-918.
- Roberts, D. H., J. A. **Klobuchar**, P. F. **Fougere**, and D. H. Hendrickson (1982). A large-amplitude traveling ionospheric disturbance produced by the May 18, 1980, explosion of Mount **St. Helens**, *J. Geophys. Res.*, 87, 6291-6301.
- Robertson, D. S., (1991). Geophysical applications of very long baseline interferometry, *Revs. Modern Phys.*, 63, 899-918.
- Rosenman, M., and S. J. Singh (1973). Quasi-static strains and tilts due to faulting in a viscoelastic half-space, *Bull. Seism. Soc. Am.*, 63, 1737-1752.
- Row, R. V. (1966). Evidence of long-period acoustic-gravity waves launched into the F regions by the Alaskan earthquake of March 28, 1964, *J. Geophys. Res.*, 71,343-345.
- Rundle**, J. B. (1978). **Viscoelastic** crustal deformation by finite quasi-static sources, *J. Geophys. Res.*, 83, 5937-5945.
- Rydelek**, P. A., and I. S. Sacks, (1990). Asthenospheric viscosity and stress diffusion - A mechanism to explain correlated earthquakes and surface deformations in NE Japan, *Geophys. Journ. Int.*, 100, 39-58.
- Sacks, I. S., A. T. Linde, J. A. Snoke, and S. **Suychiro** (1981). A slow earthquake sequence following the **Izu-Oshima** earthquake of 1978, in *Earthquake Prediction, an International Review, Maurice Ewing Ser.*, 4, 617-628, AGU, Washington D. C..
- Sasao**, T., S. **Okubo**, and M. **Saito** (1980). A simple theory on dynamical effects of stratified core upon **nutation** motions of the earth, in *Proceedings IAU Symposium 78: Nutation and the Earth's Rotation*, ed. E. P. **Federov**, M. L. Smith, and P. L. Bender, pp. 165-183, D. Reidel, Hingham, Mass..
- Saucier, F. J., E. D. Humphreys, and R. J. **Weldon, II** (1992). **Crustal** deformation in southern California from joint inversions of geologic and very long baseline interferometry measurements, *J. Geophys. Res.*, in press.
- Savage, J. C. (1983a). Strain accumulation in western United States, *Annu. Rev. Earth Planet. Sci.*, 11, 11-43.
- Savage, J. C. (1983b). A dislocation model of strain accumulation and release at a subduction zone, *J. Geophys. Res.*, 88,4984-4996.
- Savage, J. C. (1990). Equivalent strike-slip earthquake cycles in half-space and lithosphere-asthenosphere earth models, *J. Geophys. Res.*, 95, 4873-4879.
- Savage, J. C., and R. O. **Burford** (1973). Geodetic determination of relative plate motion in central California, *J. Geophys. Res.*, 78, 832-845.

- Savage, J. C., and W. H. Prescott (1973). Precision of **Geodolite distance measurements** for determining fault movements, *J. Geophys. Res.*, 78,6001-6008.
- Savage, J. C., and W. H. Prescott (1978). Asthenospheric readjustment and the earthquake cycle, *J. Geophys. Res.*, 83,3369-3376.
- Scholz, C. H., M. Wyss, and S. W. Smith (1969). Seismic and aseismic slip on the San Andreas fault, *J. Geophys. Res.*, 74,2049-2069.
- Scholz, C. H., P. Molnar, and T. Johnson (1972). Detailed studies of frictional sliding of granite and implications for earthquake mechanism, *J. Geophys. Res.*, 77,6392-6406.
- Scholz, C. H. (1988). The critical slip distance for seismic faulting, *Nature*, 336,761-763.
- Segall, P. (1991). Fault mechanics, *Rev. Geophys.*, U. S. Natl. Rep. to IUGG 1987-1990,864-876.
- Segall, P., and R. Harris (1987). Earthquake deformation cycle on the San Andreas fault near **Parkfield**, California, *J. Geophys. Res.*, 92, 10,511-10,525.
- Shibuya, K., Y. Fukuda, and Y. Michida (1990). Application of GPS relative positioning for height determination above sea level in the Antarctic marginal ice zone, *J. Phys. Earth*, 38, 149-162.
- Shimada, S., and Y. Bock, 1992. **Crustal deformation measurements in Central Japan determined by a Global Positioning System fixed-point network**, *J. Geophys. Res.*, 12,437-12,455.
- Shimada, S., S. Sakata, and S. Noguchi (1987). Cosismic strain steps observed by three-component **borehole strainmeters**, *Tectonophysics*, 144,207-214.
- Shimada, S., S. Sekiguchi, T. Eguchi, Y. Okada, and Y. Fujinawa (1989). Preliminary results of the observation by fixed-point GPS simultaneous baseline determination network in **Kanto-Tokai district**, *J. Geodetic Soc. Japan*, 35,85-95.
- Shimada, S., Y. Fujinawa, S. Sekiguchi, S. Ohmi, T. Eguchi, and Y. Okada (1990). Detection of a volcanic fracture opening in Japan using Global Positioning System measurements, *Nature*, 343, 631-633.
- Shimazaki, K., and T. Nakata (1980). Time-predictable recurrence model for large earthquakes, *Geophys. Res. Lett.*, 7, 279-282.
- Simpson, R. W., S. S. Schultz, L. D. Dietz, and R. O. Burford (1988). The response of creeping parts of the San Andreas fault to earthquakes on nearby faults: two examples, *Pageoph.*, 126,665-685.
- Singh, S. J., and M. Rosenman (1974). Quasi-static deformation of a viscoelastic half-space by **displacement dislocation**, *Phys. Earth Planet. Int.*, 8, 87-101.
- Slade, M. A., and C. F. Yoder (1989). 1960 Chile earthquake - New estimate of polar motion excitations, *Geophys. Res. Lett.*, 16, 1193-1196.
- Smith, D. E., D. C. Christodoulidis, R. Kolenkiewicz, P. J. Dunn, S. M. Klosko, M. H. Torrence, S. Fricke, S. Blackwell (1985). A global reference frame from LAGEOS ranging, *J. Geophys. Res.*, 90, 9221-9233.
- Smith, M. L. (1977). Wobble and nutation of the Earth, *Geophys. J. R. Astron. Soc.*, 50, 103-140.
- Smith, M. L., and F. A. Dahlen (1981). The period and Q of the Chandler wobble, *Geophys. J. R. Astron. Soc.*, 64, 223-281.
- Smith, S. W., and M. Wyss (1968). Displacement on the San Andreas fault subsequent to the 1966 Park field earthquake, *Bull. Seism. Soc. Am.*, 58, 1955-1973.
- Spilker, J. J. (1978). GPS signal structure and performance characteristics, *J. Inst. Navigation*, 25, 121-146.
- Stacey, F. D. (1977). *Physics of the Earth*, 2nd ed., John Wiley and Sons, Inc., New York, 414 pp.
- Starr, A. T. (1928). Slip in a crystal and rupture in a solid due to shear, *Proc. Cambridge Phil. Soc.*, 24, 489-500.
- Stein, S., and R. J. Geller (1977). Time domain observation and synthesis of split spheroidal and torsional free oscillations of the 1960 Chilean earthquake: **Preliminary results**, *Bull. Seism. Soc. Am.*, 68, 325-332.
- Sykes, L. R., and R. C. Quittmeyer (1981). Repeat times of great earthquakes along simple plate boundaries, in Earthquake Prediction, ed. D. W. Simpson, and P. G. Richards, pp. 217-247, Washington, D. C., Am. Geophys. U., 680 pp.
- Tajima, F., and D. M. Tralli (1991). Variation of seismic slip in the Gulf of California and possible effect on geodetic measurements of Pacific-North America plate motion, *J. Geophys. Res.*, 97,4903-4913.
- Tapley, B. D., B. E. Schutz, and R. J. Eanes (1985). Station coordinates, baselines, and earth rotation from LAGEOS laser ranging: 1976-1984, *J. Geophys. Res.*, 90, 9235-9248.

- Thatcher, W. (1975). Strain accumulation and release mechanism of the 1906 San Francisco earthquake, *J. Geophys. Res.*, 80,4862-4872.
- Thatcher, W. (1979). Systematic inversion of geodetic data in central California, *J. Geophys. Res.*, 84, 2283-2295.
- Thatcher, W., and J. B. Rundle (1984). A viscoelastic coupling model for the cyclic deformation due to periodically repeated earthquakes at subduction zones, *J. Geophys. Res.*, 89,7631-7640.
- Tralli, D. M., T. H. Dixon, and S. A. Stephens (1988). The effect of wet tropospheric path delays on estimation of geodetic baselines in the Gulf of California using the Global Positioning System, *J. Geophys. Res.*, 93,6545-6557.
- Tralli, D. M., and S. M. Lichten (1990). Stochastic estimation of tropospheric path delays in Global Positioning System geodetic measurements, *Bull. Geod.*, 64, 127-159.
- Tralli, D. M. (1991). Spectral comparison of continuous Global Positioning System and strainmeter measurements of crustal deformation, *Geophys. Res. Lett.*, 18, 1285-1288.
- Tse, S. T., and J. R. Rice (1986). Crustal earthquake instability in relation to the depth variations of frictional slip properties, *J. Geophys. Res.*, 91, 9452-9472.
- Tunis, T. E. (1988). Rock friction constitutive behavior from laboratory experiments and its implications for an earthquake prediction field monitoring program, *Pageoph.*, 126,555-588.
- Turcotte, D. L., and D. A. Spence (1974). An analysis of strain accumulation on a strike-slip fault, *J. Geophys. Res.*, 79,4407-4412.
- Turcotte, D. L., R. T. Clancy, D. A. Spence, and F. H. Kulhawy (1979). Mechanisms for the accumulation and release of stress on the San Andreas fault, *J. Geophys. Res.*, 84, 2273-2282.
- Turcotte, D. L., and G. Schubert (1982). *Geodynamics*, John Wiley, New York, 450 pp.
- Vasco, D. W., L. R. Johnson, and N. E. Goldstein (1988). Using surface displacement and strain observations to determine deformation at depth, with an application to Long Valley Caldera, California, *J. Geophys. Res.*, 93, 3232-3242.
- Wahr, J. M. (1981). The forced nutations of an elliptical, rotating, elastic and oceanless earth, *Geophys. J. R. Astron. Soc.*, 64, 705-727.
- Ward, S. N. (1985). Quasi-static propagator matrices: Creep on strike-slip faults, *Tectonophysics*, 120,83-106.
- Ward, S. N. (1988). North America-Pacific plate boundary, an elastic-plastic megashear: Evidence from very long baseline interferometry, *J. Geophys. Res.*, 93,7716-7728.
- Ward, S. N., and S. E. Barrientos (1986). An inversion for slip distribution and fault shape from geodetic observations of the 1983, Borah Peak, Idaho, earthquake, *J. Geophys. Res.*, 91,4909-4919.
- Wesson, R. L. (1988). Dynamics of fault creep, *J. Geophys. Res.*, 93, 8929-8951.
- Wiggins, R. A. (1972). The general linear inverse problem: Implication for surface waves and free oscillations for earth structure, *Rev. Geophys.*, 10, 251-285.
- Williams, P. L., and S. F. McGill, K. E. Sieh, C. R. Allen, and J. N. Louie (1988). Triggered slip along the San Andreas fault after the 8 July 1986 North Palm Springs earthquake, *Buff. Seism. Soc. Am.*, 78, 1112-1122.
- Wolcott, J. H., D. J. Simons, D. D. Lee, and R. A. Nelson (1984). Observations of an ionospheric perturbation arising from the Coalinga earthquake of May 2, 1983, *J. Geophys. Res.*, 89,6835-6839.
- Wyatt, F. K. (1988). Measurements of coseismic deformation in southern California: 1972-1982, *J. Geophys. Res.*, 93, 7923-7942.
- Xie, X. B., and Z. X. Yao (1991). The faulting process of Tangshan earthquake inverted simultaneously from the teleseismic waveforms and geodesic deformation data, *Phys. Earth Planet. Int.*, 66,265-277.
- Yabuki, T., T. Kanazawa, and H. Wakita (1991). Anomalous movements in Oshima volcano associated with the Off Ito submarine eruption revealed from GPS measurements, *J. Phys. Earth*, 39, 155-164.
- Yoshida, S., and K. Koketsu (1990). Simultaneous inversion of waveform and geodetic data for the rupture process of the 1984 Naganoken-Seibu, Japan, earthquake, *Geophys. J. Int.*, 103,355-362.
- Yuen, P. C., P. F. Weaver, R. K. Suzuki, and A. S. Furumotu (1969). Continuous, traveling coupling between seismic waves and the ionosphere evident in May 1968 Japan earthquake data, *J. Geophys. Res.*, 74,2256-2264.

Figure Captions

- Fig. 1. (Top): Range of linear dimensions of an earthquake ($M > 6$) and baseline lengths involved in GPS, VLBI and SLR measurements. (Bottom: Time spans typical for an earthquake source process and space-based geodetic measurements (**GPS, VLBI and SLR**)). Dashed lines indicate ranges (yet ambiguous) associated with **preseismic** and post seismic deformation. Dotted lines and arrows show potential application ranges for each technique.
- Fig. 2. (a) Geometry of an earthquake **fault** and observation point. (ξ_1, ξ_2, ξ_3) is the rupture front coordinate on the fault **plane** and (x_1, x_2, x_3) is the observation point. (b) Grids are allocated on the fault plane to model the rupture process as a series of point sources.
- Fig. 3. Diagram of a simple screw dislocation model for a shallow, strike-slip, vertical fault. The dashed circle is displaced to the solid, and a uniform relative displacement of S results on the fault surface (figure taken from *Stacey* [1977]).
- Fig. 4. (a) Simple uniform elastic **halfspace** and (b) elastic layer over **viscoelastic halfspace** models used to describe the earthquake cycle. The bold lines to a depth D in (a) and to a depth H in (b) denote the extent of coseismic rupture. The response in (b) is given by *Nur and Mavko* [1974] (for further discussions, see *Savage and Prescott* [1978] and *Savage* [1990]).
- Fig. 5. Geometry of a simple vertical rectangular fault, with a strike-slip source of length $2L$ extending from depths h to H below the free surface, in an isotropic, linearly viscoelastic **halfspace** (from *Rosenman and Singh* [1973]).
- Fig. 6. a) The variation of the **fault-parallel** strain component ϵ_{xx} with epicentral distance along the fault. The ratio H/L is 0.1 (see Fig. 5) **Voigt** and **Maxwell viscoelastic model** cases are shown for comparison, and coincide with the elastic case for zero and infinite respective relaxation times: b) same as a) for the **fault-perpendicular** strain component ϵ_{yy} with epicentral distance perpendicular from the fault (from *Rosenman and Singh* [1973]).
- Fig. 7. Schematic locations of the GPS network in the **southern** Gulf of California [*Dixon et al.*, 1991b] and the four model transform events used for numerical calculations of surface displacements (from *Tajima and Tralli* [1991]). The faults extend from the surface to a depth of 10 km, with a prescribed dislocation of 1 m and assumed rigidity of 3×10^{11} dyne/cm², yielding a seismic moment of 1.5×10^{26} dyne-cm. The fault model geometry is shown in Fig. 6. Surface displacements are shown in Fig. 8.
- Fig. 8. East-west surface displacements relative to **Cabo San Lucas**, as a function of distance along the 450 km baseline from **Cabo San Lucas** to **Bahia de Concepcion**, due to the model events shown in Fig. 7. All events are assumed in an elastic **halfspace** unless otherwise indicated. Maxwell viscoelastic model displacements are specified with t/τ equal to 1. The dotted lines indicate the geodetic precision of GPS measurements determined from the actual GPS network based on **repeatabilities** (random errors), while dashed lines are the total errors which include systematic errors based on sensitivity analyses [*Dixon et al.*, 1991b]).
- Fig. 9. Plot of the characteristic time versus characteristic length of lithospheric deformation events. Creep events on the San Andreas fault occur at approximately 1 m/s and strain migration events occur at about 1 mm/s (from *Beroza and Jordan* [1990]).
- Fig. 10. Schematic diagram of the three space-based geodetic techniques discussed in the text (figure adopted from *D. Wells* (1987), Guide to GPS positioning, Canadian GPS Associates).
- Fig. 11. Geographic location of the automated fixed-point GPS network installed in the south **Kanto-Tokai** region surrounding Tokyo by Japan's National Research Center for Disaster Prevention (from *Shimada et al.*, [1990]),

Fig. 12. Change in the components of a 10 km baseline overlying the **Teishi** undersea volcano (see Fig. 10). After the **peak** of the seismic swarm prior to the eruption, a 10 cm change in N-S and 8 cm change in E-W baseline components was observed, with an overall baseline length extension of about 10 cm (adopted from *Shimada et al.*, [1990]).

Fig. 13. Schematic log-log power spectral density diagram **comparing strainmeter** measurements with 5 and 1 day GPS geodetic sampling, and continuous GPS measurements. **f_N** refers to a **Nyquist frequency** and **f_c** to a crossover frequency (see Eq. (8.3)), and **f_c** to a corner frequency for correlated noise [Tralli, 1991].

Fig. 14a. GPS geodetic baseline error as a function of length using the model given by Eq. (8.4), with **a** equal to 0.1 cm, **b** equal to 3 parts in 10⁸ and:

	c (cm)	λ (km)
I, Ha	0.5	100
IIb	0.5	50
IIIa	1.0	100
IIIb	1.0	50

Fig. 14b. Comparison of the crossover time (days) after which GPS measurements of **crustal** deformation yield a smaller relative noise level than **strainmeters**, as a function of baseline length, for errors as given in Fig. 14a with **I**) $\Delta t=5$ days; **II**) $\Delta t=1$ day; and **III**) $\Delta t=0.5$ day in Eq. (8.3). **Strainmeter** model **parameters** are described in Section 8.1.

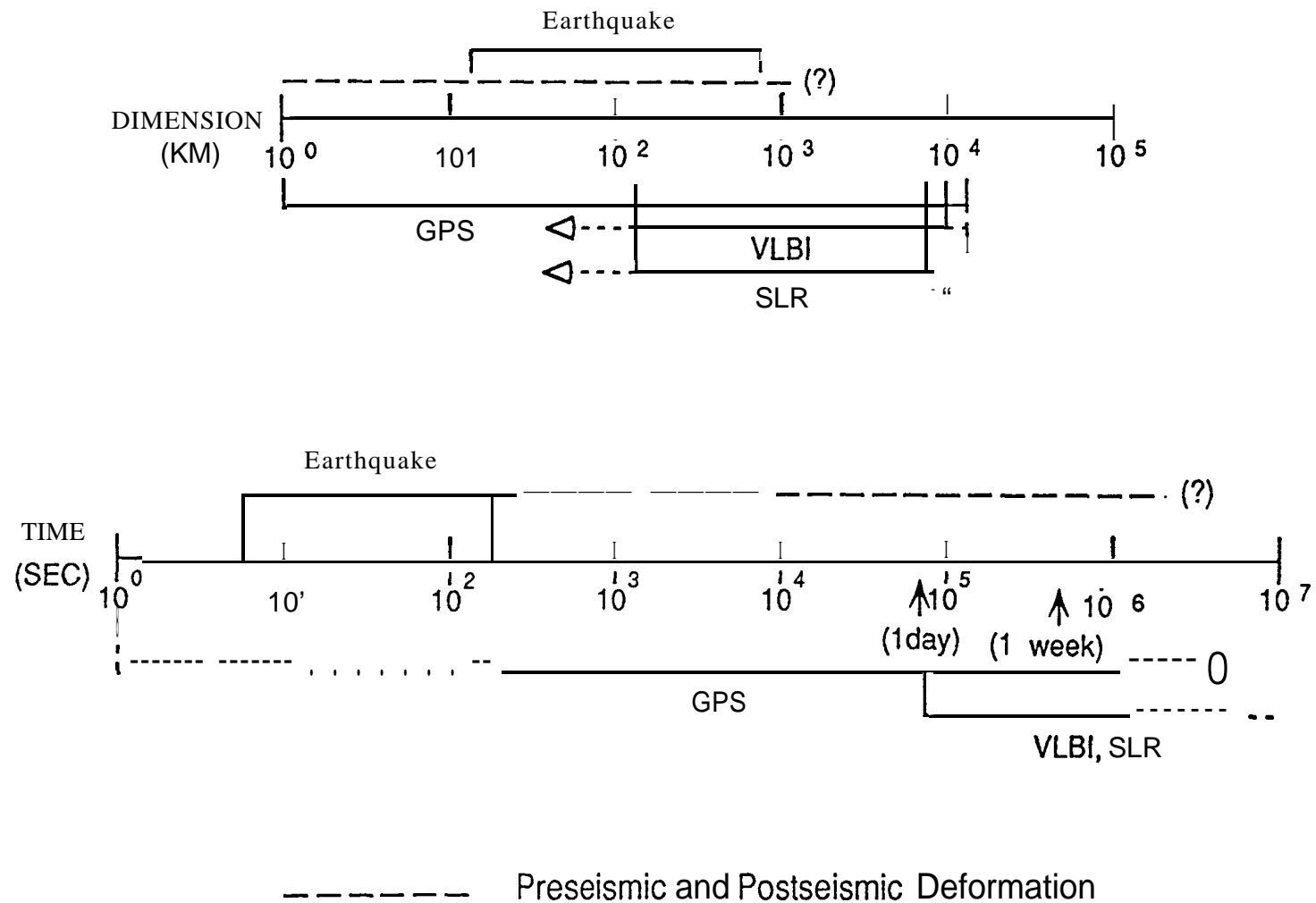


Figure 1

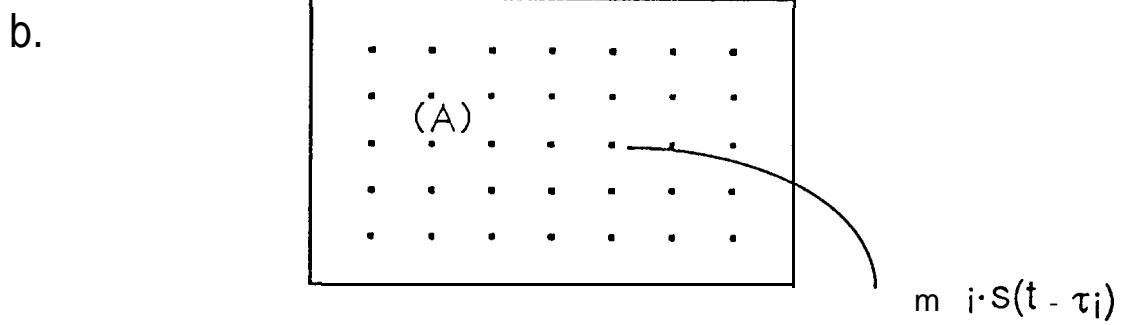
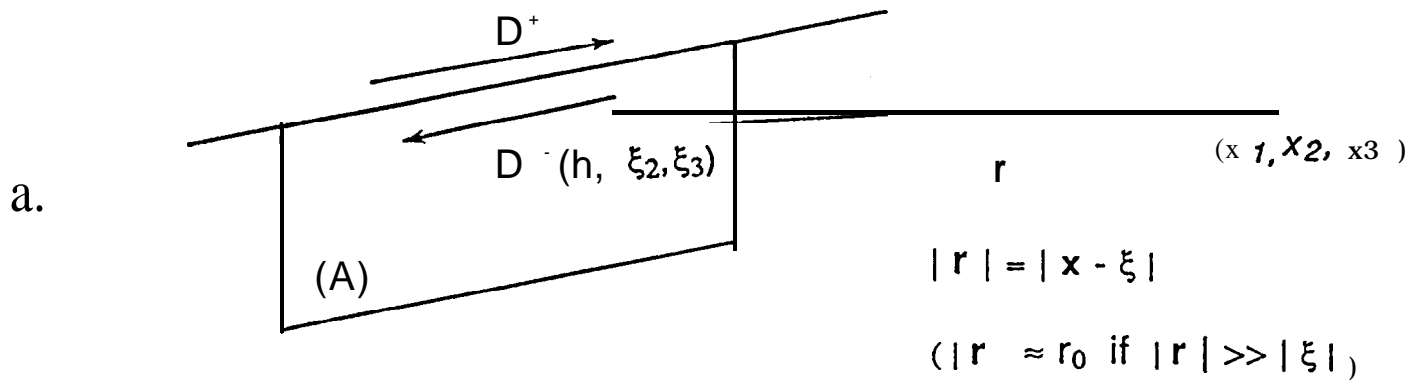


Fig. 2

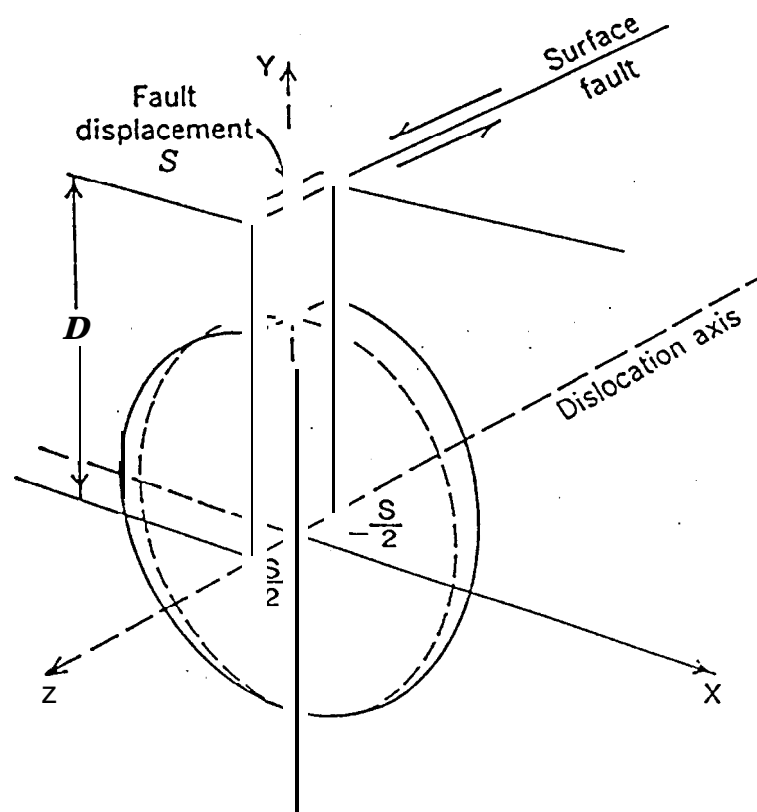
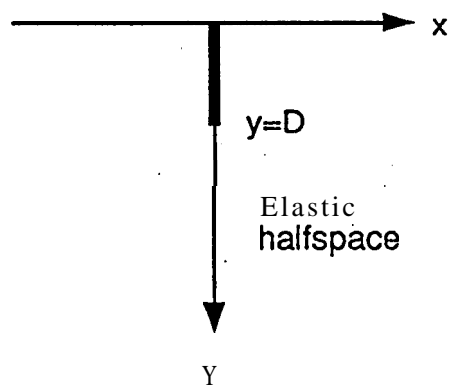


Fig. 3

a) Uniform halfspace model



b) Lithosphere-asthenosphere model

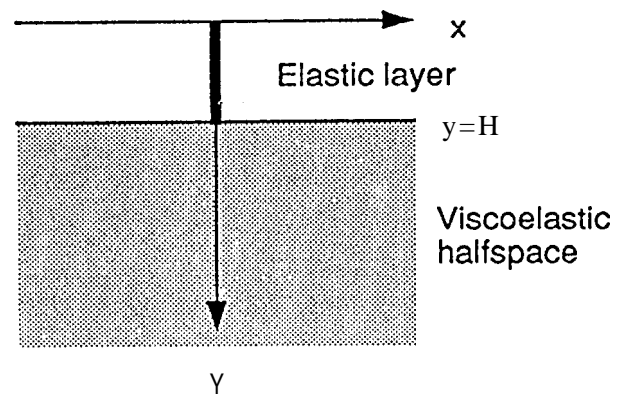


Figure 4

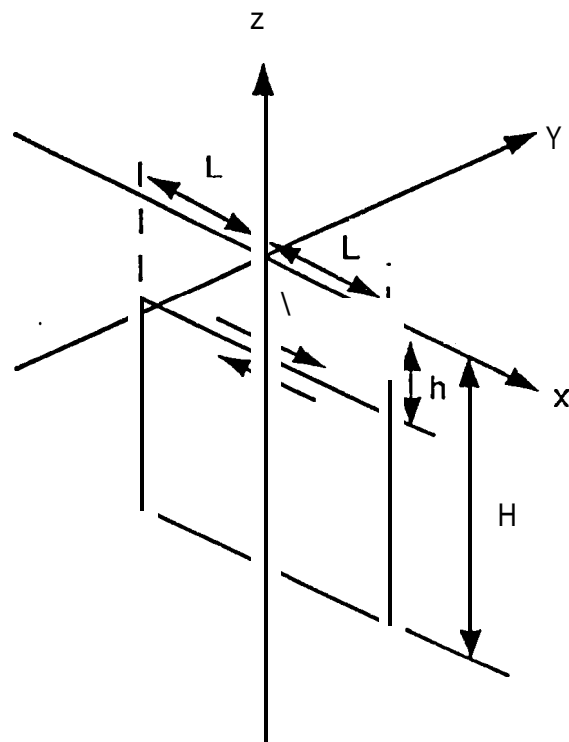


Figure 5

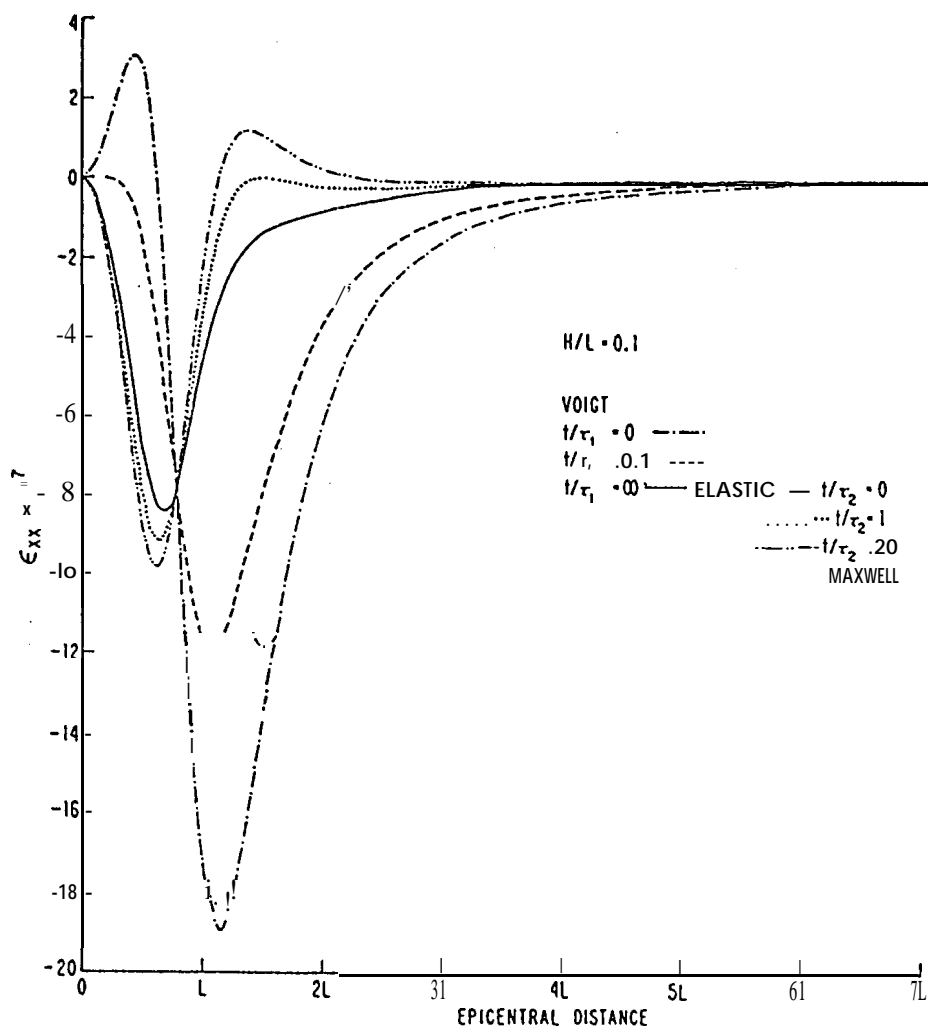


Fig. 6

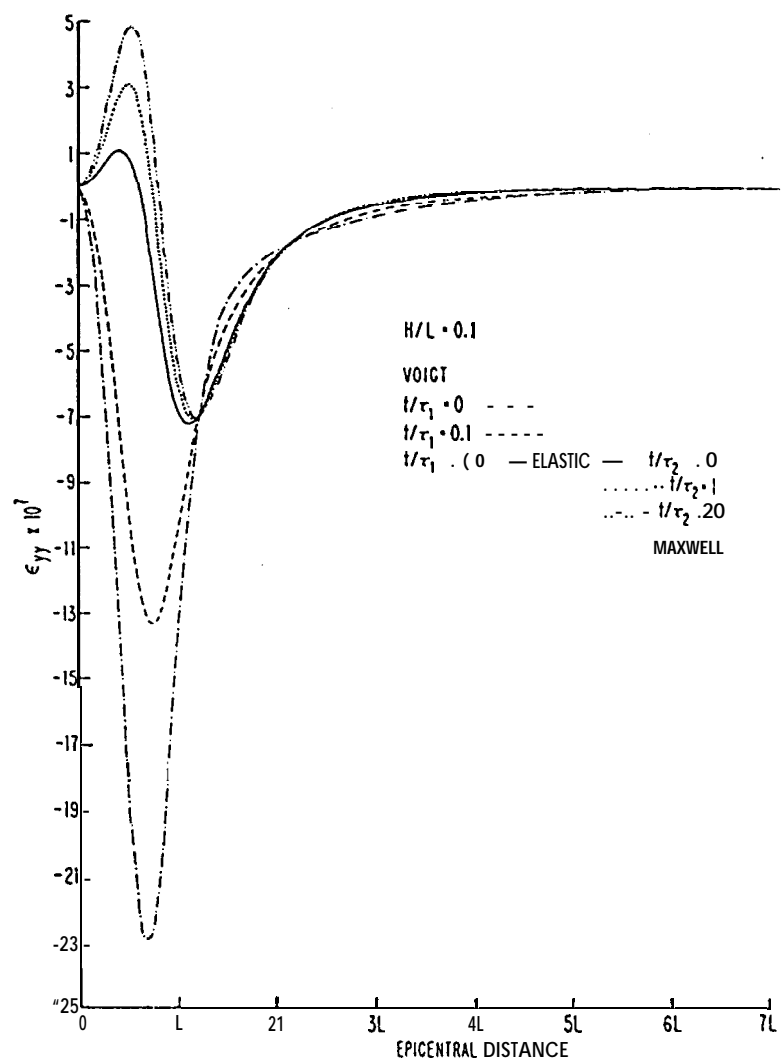


Fig. 6b

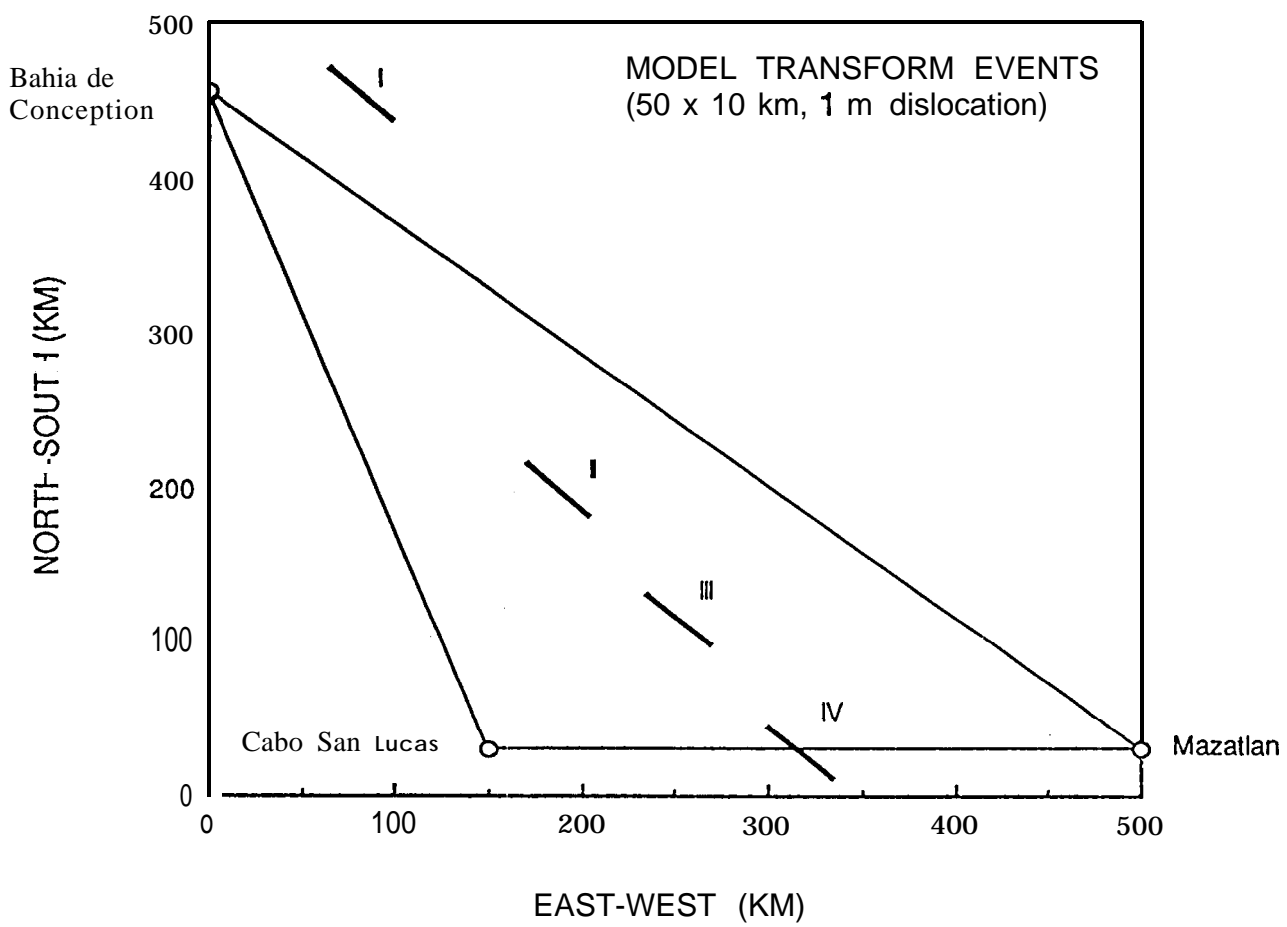
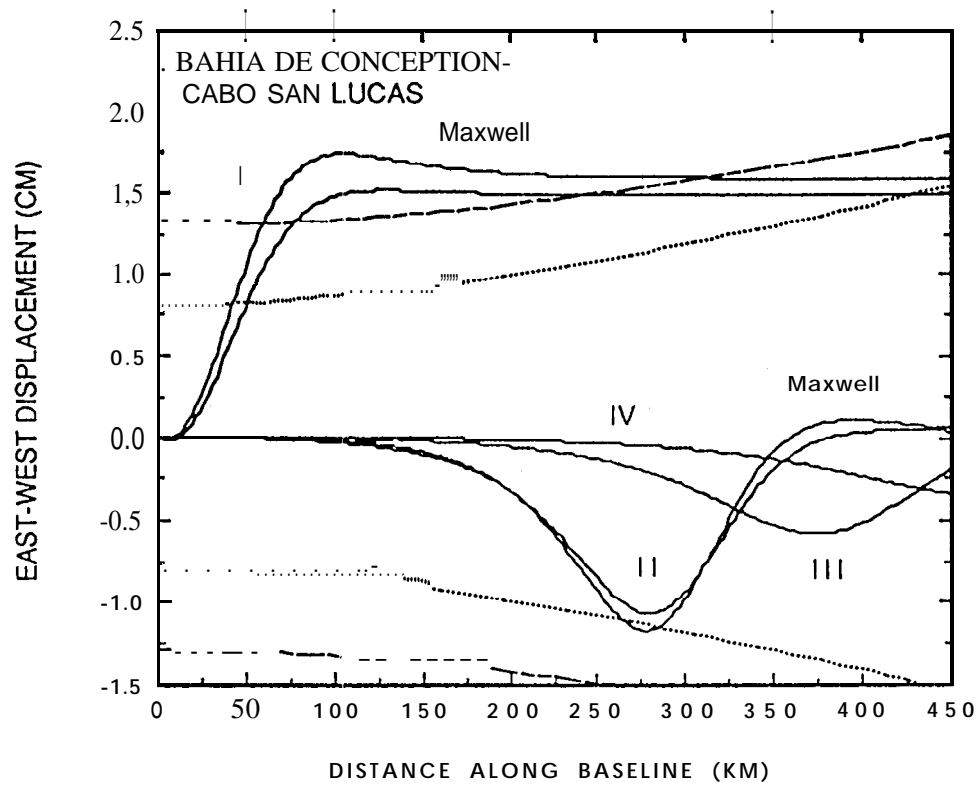


Figure 7



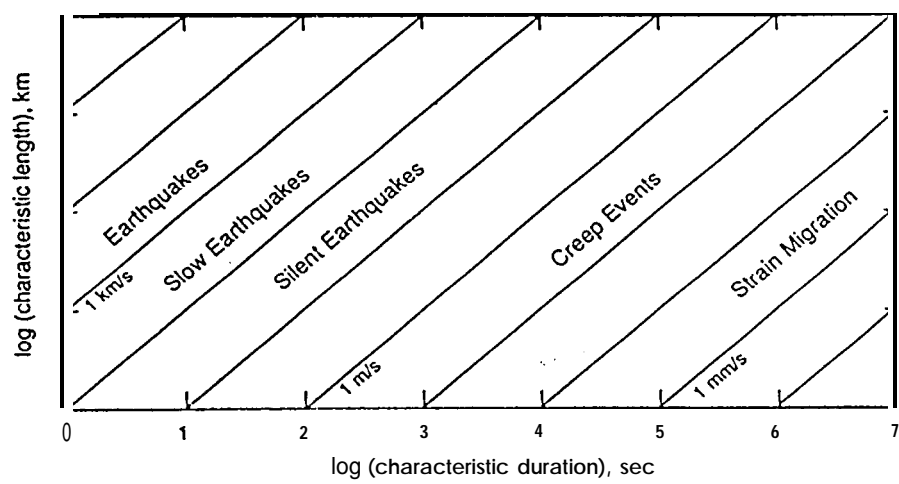


Fig. 9

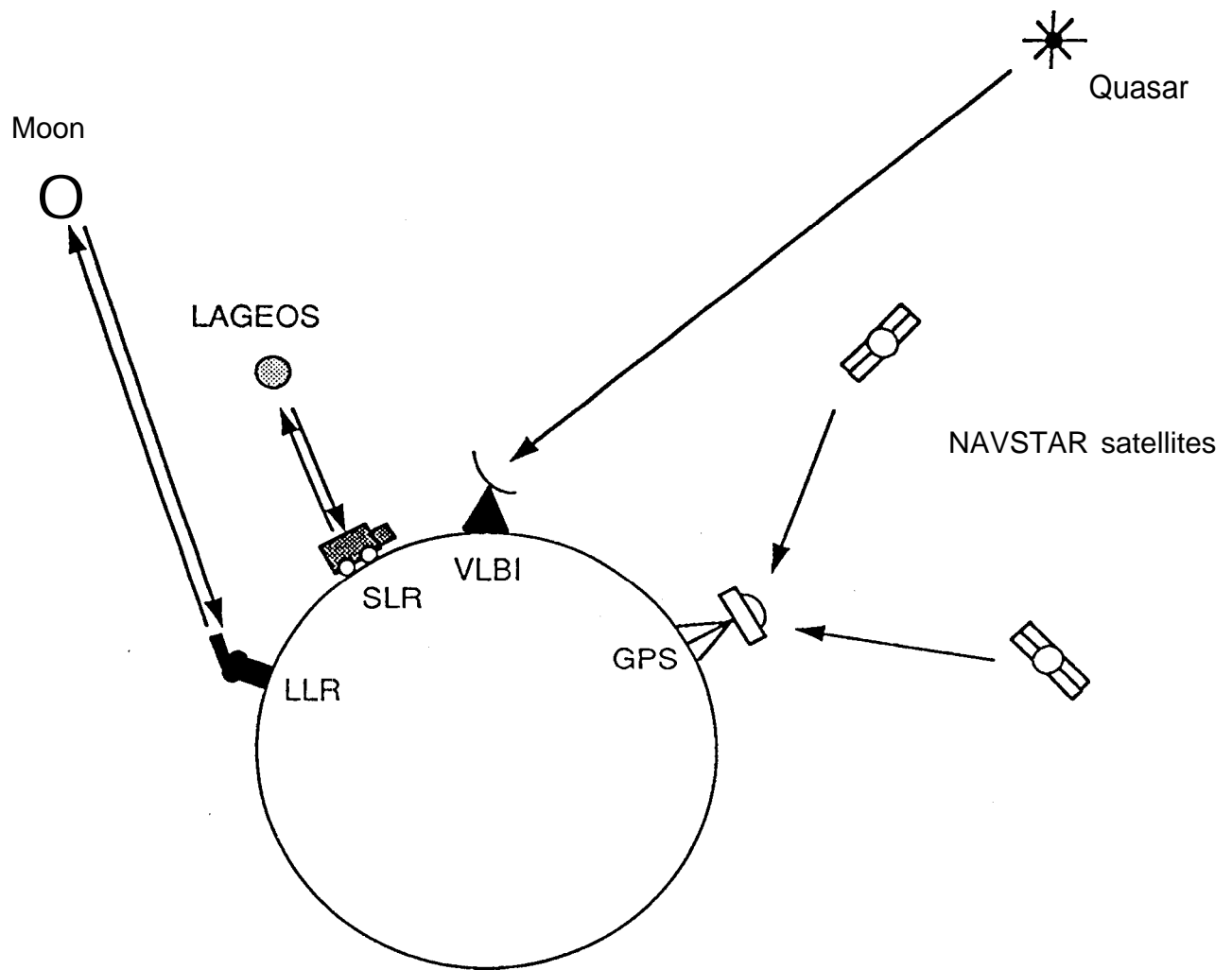


Figure 10

ITO POSITION RELATIVE TO HTS

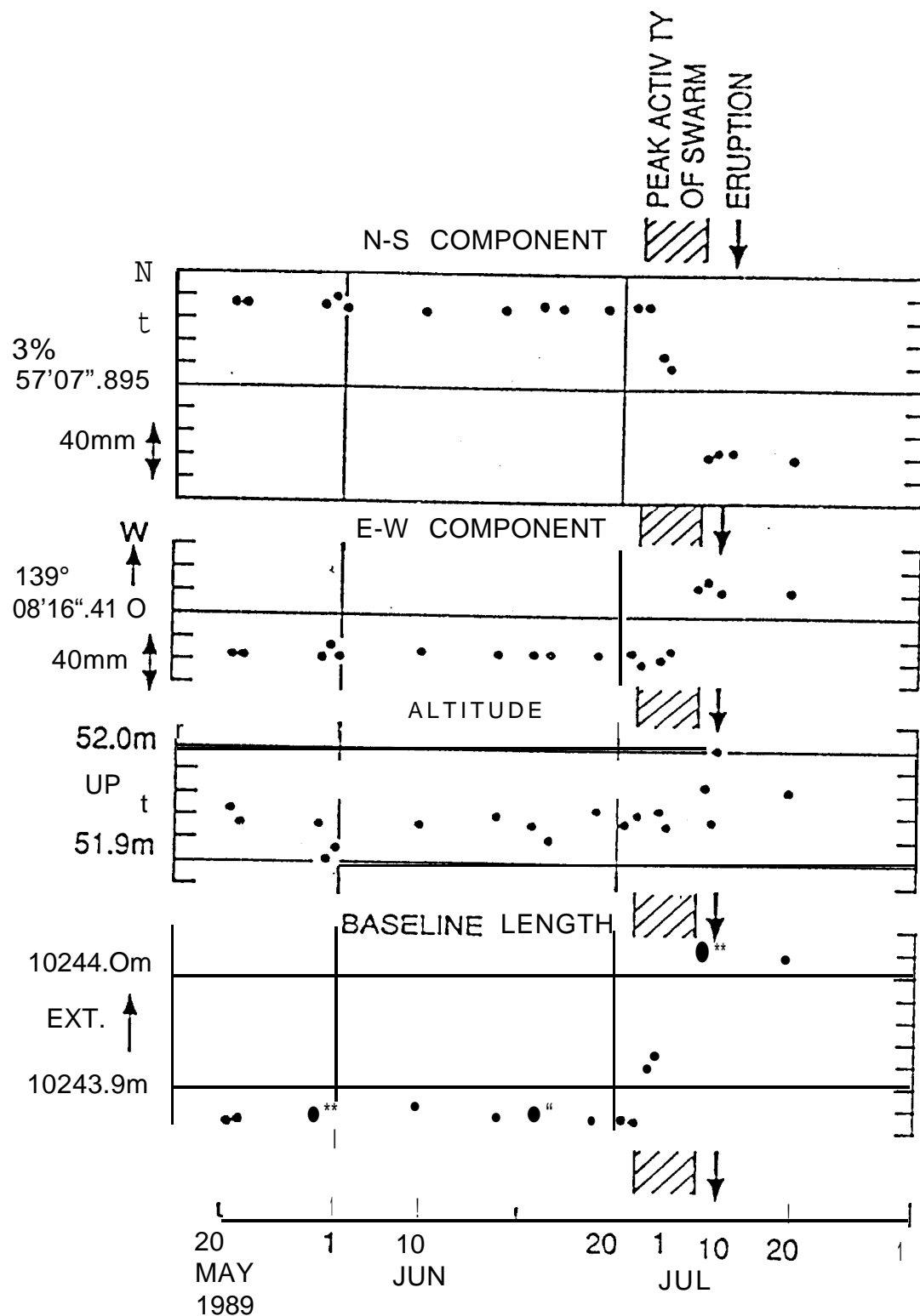


Fig. 12

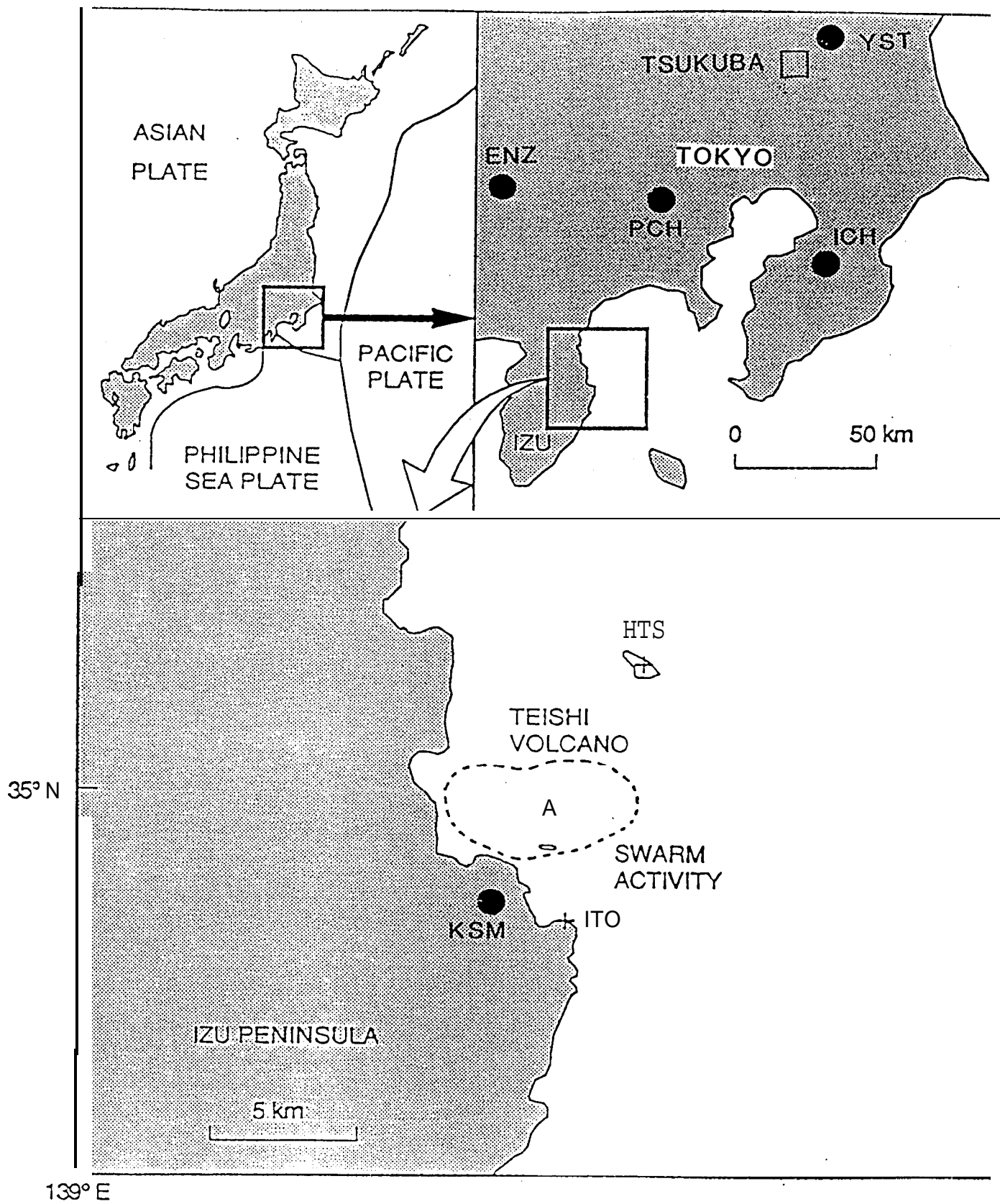


Fig. 1

ITO POSITION RELATIVE TO HTS

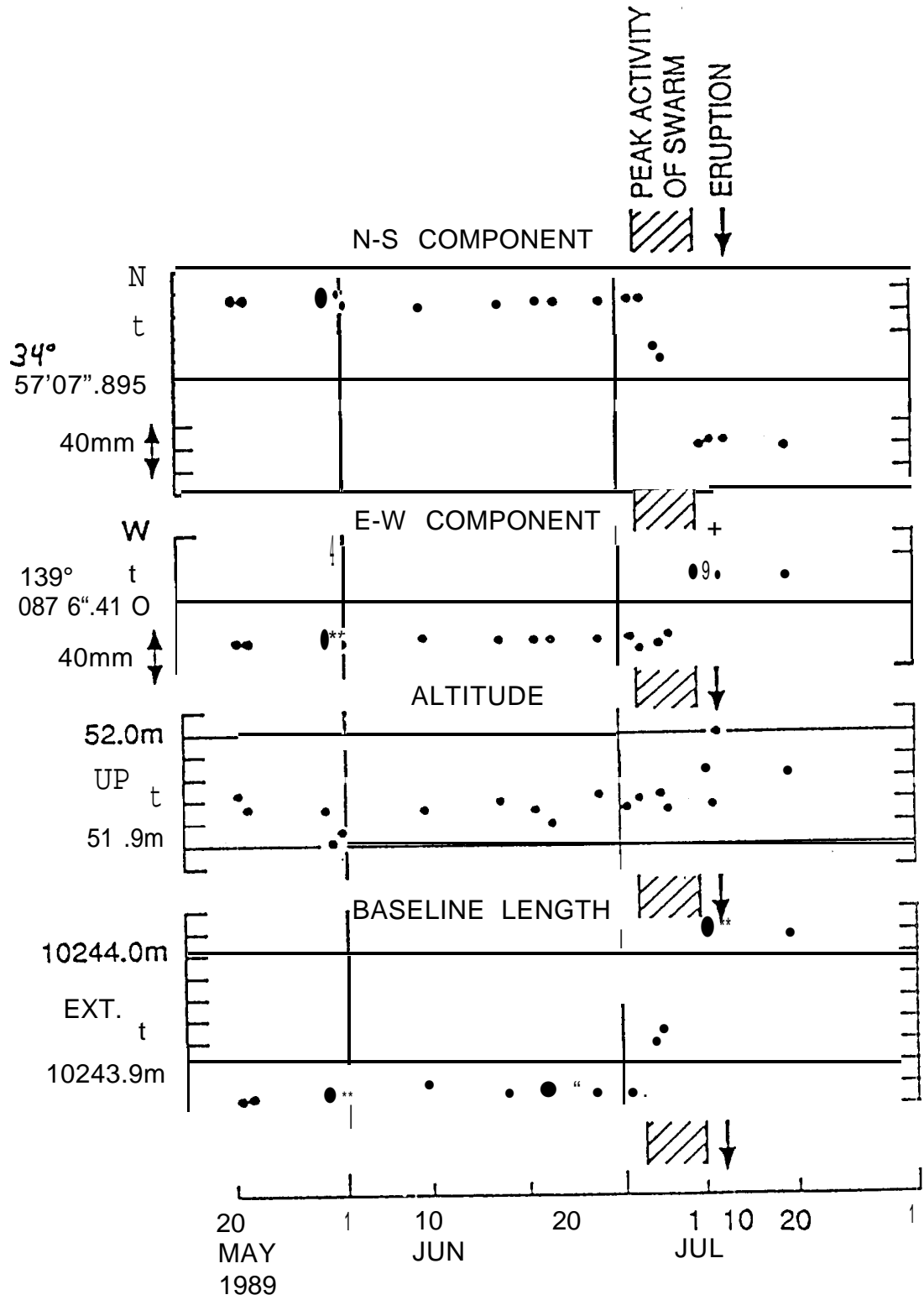


Fig. 1

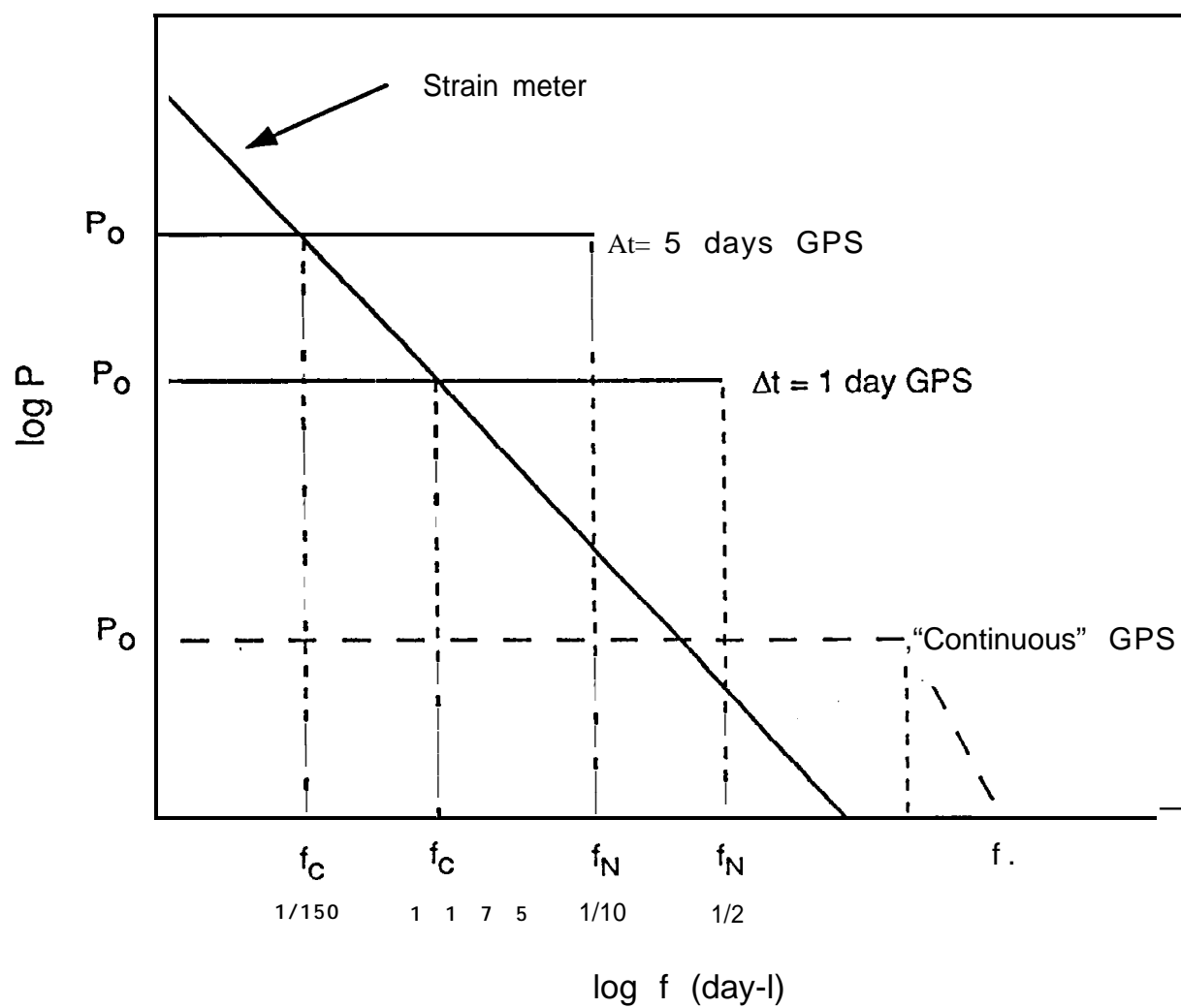


Figure 13

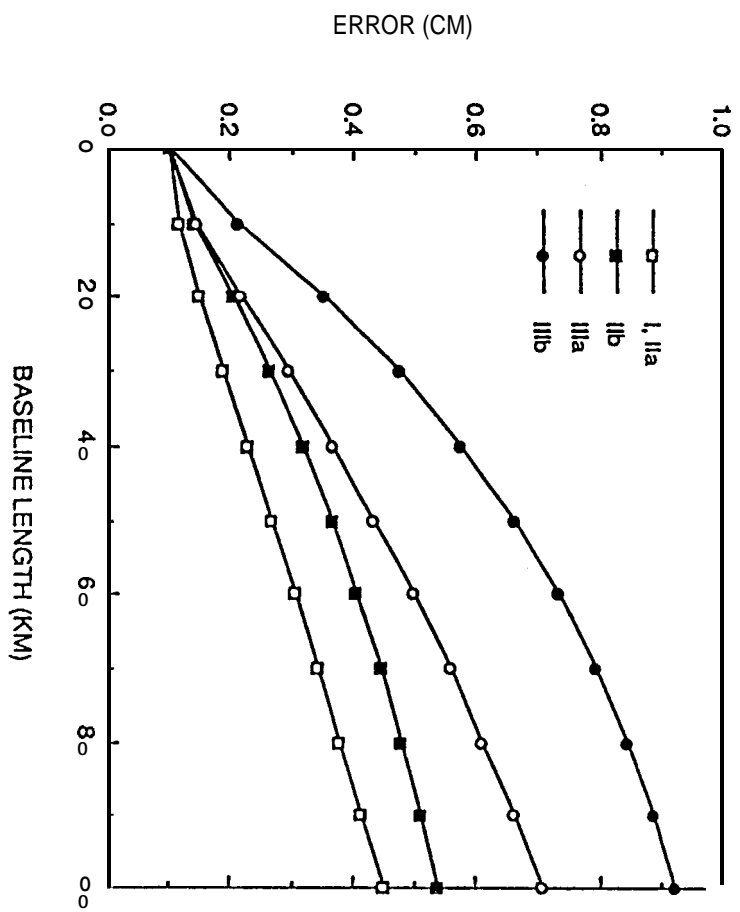


Fig. 14a

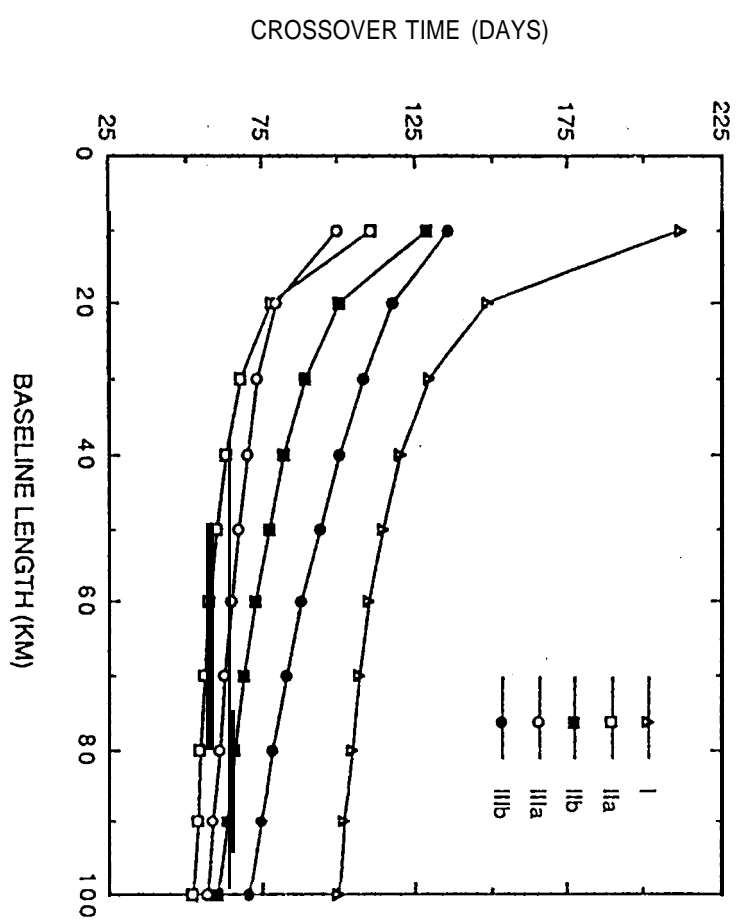


Fig. 14b